M-Voronoi and other random open and closed-cell elasto-plastic cellular materials: Geometry generation and numerical study at small and large strains

Z Hooshmand-Ahoor, H Luo, K Danas

International Journal of Solids and Structures 290 (2024) 112680

Contents lists available at ScienceDirect

International Journal of Solids and Structures

journal homepage: www.elsevier.com/locate/ijsolstr

M-Voronoi and other random open and closed-cell elasto-plastic cellular materials: Geometry generation and numerical study at small and large strains

Z. Hooshmand-Ahoor [a], H. Luo [a], K. Danas [a,b,*]

[a] LMS, C.N.R.S., École Polytechnique, Institut Polytechnique de Paris, 91128 Palaiseau, France
[b] ELyTMaX, CNRS, Tohoku University, Sendai, Japan

ARTICLE INFO

Keywords:
Architected materials
Random geometries
Voronoi materials
Disordered porous materials
Void growth
Finite strain simulations
Computational morphogenesis
Foams

ABSTRACT

The present study deals with a numerical design strategy of a novel class of three-dimensional random Voronoi-type geometries, called M-Voronoi. These materials comprise random, non-quadratic convex void shapes and non-uniform intervoid ligament thicknesses, and can span high-to-low relative densities. The starting point for their generation is a random adsorption algorithm (RSA) construction with spherical voids embedded in an incompressible, nonlinear elastic matrix phase. The initial RSA geometry is subjected to large elastic volume changes by prescribing Dirichlet boundary conditions. Due to the incompressibility of the matrix phase, the externally imposed volume changes lead to significant void growth. The numerical growth process may be stopped at any desired porosity. The proposed M-Voronoi process is general and allows the formation of isotropic (or anisotropic) designs. As a byproduct of the developed approach, we also present a novel remeshing technique allowing to read arbitrary geometries of one or multiple phases. The elasto-plastic properties of the M-Voronoi porous materials are numerically investigated at small strains as well as large compressive and shear loads. Their response is assessed by comparison with other well-known random and periodic porous geometries such as polydisperse porous materials with spherical voids (RSA), classical TPMS Gyroid geometries and random Spinodoid topologies. The results show that M-Voronoi and RSA (with spherical voids) geometries exhibit the stiffest elastic and highest flow stress response compared to the other two geometries. This study shows unambiguously that randomness may or may not lead to enhanced mechanical response such as higher stiffness or flow stress.

1. Introduction

Cellular solids can have a wide range of small-scale topological architecture, ranging from the nearly perfect order seen in honeycombs to the disordered, three-dimensional networks found in sponges and foams. The characteristics of porous materials can be classified in a variety of ways. Starting from purely topological characteristics, they can be classified into periodic or random. Periodic cellular materials have been studied since the 1950s (or perhaps for centuries), with extensive experimental and theoretical investigations on the influence of the primitive cell geometry. In those studies, it has become crystal clear that instabilities appear almost always, leading to deformation localization as well as short or long wavelength buckling of the ligaments (Papka and Kyriakides, 1998; Combescure et al., 2016, 2020; Balit et al., 2021; Dong et al., 2015; Andrew et al., 2021; Luan et al., 2022). These instabilities may be further exacerbated when using 3D printing fabrication techniques due to imperfections inherent in the printing process. Imperfections can significantly degrade the elastic moduli and subsequent nonlinear behavior of these lattices, leading to experimental responses that deviate significantly from the original design and numerical predictions (Symons and Fleck, 2008; Fu and Xie, 2012). Additionally, periodic cellular materials exhibit in most cases direction-dependent mechanical properties and inherent orthotropy or anisotropy at finite strains (even if some of them may be isotropic in small elastic strains), which can be problematic, especially when structures are subjected to unknown loading conditions. Finally, their periodicity may be problematic since it may be non-conformal with the macroscopic geometry of the structure that needs to be designed.

While regular periodic patterns are common in periodic geometries, Triply Periodic Minimal Surface (TPMS) structures derived from the minimum surface condition with zero mean curvature exhibit more intricate and complex periodic features. TPMS structures originated

* Corresponding author at: LMS, C.N.R.S., École Polytechnique, Institut Polytechnique de Paris, 91128 Palaiseau, France.
E-mail address: konstantinos.danas@polytechnique.edu (K. Danas).

https://doi.org/10.1016/j.ijsolstr.2024.112680
Received 25 October 2023; Received in revised form 17 January 2024; Accepted 19 January 2024
Available online 20 January 2024

from the study of Schoen (1970) and Schwarz (1972) are designed by use of very simple mathematical expressions and can reach fairly low densities (Soyarslan et al., 2019). They are promising candidates for multifunctional material design due to their smooth curvature and potential for functionally graded structures. Moreover, the TPMS-like shell-lattice structures are stronger and more stable than most of periodic structures including octet trusses. However, their inherent cubic symmetry can be a limitation when exposed to multi-directional loading (Bonatti and Mohr, 2019) or more complex structures need to be created with such materials.

In contrast to periodic cellular materials, natural porous materials and biological tissues commonly comprise random topology (Gaitanaros et al., 2012). Even materials often considered periodic, like bee honeycombs, exhibit irregularities, with varying void sizes and shapes, potentially leading to gradient porosity and mechanical properties (Ashby and Gibson, 1997). The complexity of structural topology in random cellular materials makes their geometry realization very challenging (Su and Jang, 2022). Several structural models have been developed by replacing the actual random topology with those that have simpler periodic or random geometries. However, these approaches have limitations. First, they lack microstructural characteristics such as random cell size, shape, orientation, and position. Secondly, they often lead to instabilities and direction-dependent properties, which make their response far from that of a random geometry (see Warren and Kraynik (1997) for liquid foams, and Simone and Gibson (1998) for metal foams). A popular method for numerically constructing random foams involves tomography scanning of actual microstructures, producing precise random geometries. This technique relies on X-ray computed tomography scans to characterize these microstructures (Amani et al., 2018; Ghazi et al., 2020; Wang et al., 2021) and thus requires repeated scanning for numerical analysis, which is extremely time consuming.

Many studies have explored methods for generating random geometries. A classic approach involves microstructures with randomly distributed spherical voids created using random sequential adsorption (RSA) or random closed packing (RCP) methods (Lubachevsky et al., 1991; Torquato, 2002). Modifications to the RSA algorithm have expanded its versatility. Segurado and Llorca (2002) adjusted the algorithm to produce RSA geometries with periodic unit-cell boundaries while maintaining minimal void distances. Pierard et al. (2007) extended it to generate random monodisperse ellipsoidal inclusions. Lopez-Pamies et al. (2013) proposed a modification for constructing polydisperse microstructures with various particle sizes. Anoukou et al. (2018) presented a comprehensive RSA algorithm encompassing all these features, using an iterative numerical approach to determine minimum inclusion distances. It is essential to note that non-overlapping RSA geometries have limitations in terms of inclusion volume fractions (or porosity). Due to the irreversible nature of the sequential process, achieving high volume fractions while avoiding overlap is challenging. An even greater challenge arises if the inclusions are monodisperse. In this case, the maximum volume fraction approximately corresponds to 0.38 and 0.55 for 3D and 2D RSA, respectively (Feder, 1980; Cooper, 1988). To surpass these limits, either one starts with small volume fractions and grows the sphere sizes (see for instance Lubachevsky and Stillinger 1990 and de Francqueville et al. 2019) to reach monodisperse closely packed microstructures of larger volume fraction ~0.64 or instead use polydisperse distributions with smaller inclusions to reach even higher volume fractions. Even then, achieving inclusion/void concentrations beyond 0.8 in 3D and 0.9 in 2D remains highly challenging and demands an extremely large number of inclusions (in the order of tens of thousands) of very different sizes. Manufacturing considerations may also play a role if one decides to manufacture such porous materials, as the minimum inclusion distance is dictated by 3D printing accuracy (Zerhouni et al., 2019). This constraint leads to a substantial small-to-large void size ratio (Tarantino et al., 2019), resulting in significant polydispersity at high inclusion volume fractions, which is simply non-realizable with current 3D-printing technology nor is possible to simulate such geometries, especially at finite strains at a finite time scale.

Another type of random porous geometries includes Voronoi tessellations generated using the Laguerre-Voronoi diagram algorithm (Wejrzanowski et al., 2013), which divides space into polyhedral cells with constant but non-zero thickness and variable length (Spyrou et al., 2019). Voronoi geometries are commonly used in simulating polycrystalline microstructures or foams (Gaitanaros and Kyriakides, 2015; Gahlen and Stommel, 2022; Gong and Kyriakides, 2005). However, when considering porous Voronoi geometries, it is essential to note their limitations, namely, the absence of variable cell wall thickness and smooth corners. These limitations render Voronoi tessellation geometries susceptible to localized deformation at finite strain loading and lead to deformation modes similar to periodic ones (Hooshmand-Ahoor et al., 2022), especially at higher relative densities >0.1.

Spinodoid topology is another type of random geometries introduced recently by Soyarslan et al. (2018), Hsieh et al. (2019) and Kumar et al. (2020). These geometries are obtained through specific spinodal phase separation by Gaussian random fields (GRF) and can be connected to the solution of the famous Cahn–Hilliard diffusion problem (Geslin et al., 2019). Spinodoid or in general Gaussian-type topologies exhibit a non-optimal mechanical response (Roberts and Garboczi, 2001; Zerhouni et al., 2021) when compared with available mathematical bounds in linear elasticity. Moreover, they cover a limited density span ranging approximately between 0.7 and 0.2 (Maskery et al., 2017), unless spinodoid shell models are employed. In the latter case, the interface between the solid and void phases is assumed to be a solid shell (Hsieh et al., 2019). Despite of these drawbacks, their simple mathematical construction offers the versatility of tailored isotropic and anisotropic responses through inverse design processes (Kumar et al., 2020).

1.1. Scope of the study

The goal of the present work is twofold. The first is to propose a novel design of mechanically grown Voronoi-type materials, called M-Voronoi, with random smooth topological features involving both void shapes and intervoid ligament thickness. This is achieved by finite strain simulations of a unit-cell of an incompressible neo-Hookean matrix comprising initially randomly distributed spherical voids. The void growth is triggered by applying volume increase Dirichlet boundary conditions on the outer boundary of the unit-cell. The second goal is to analyze the M-Voronoi microstructure and probe the effect of randomness on the linear and elasto-plastic properties of such geometries numerically. To assess the M-Voronoi response, we also analyze three additional microstructures; polydisperse RSA with spherical voids, Gyroid TPMS and Spinodoid geometries at various relative densities.

This paper is organized as follows. In Section 2, the general numerical design process of the M-Voronoi geometries is presented in detail including initial RSA geometry, nonlinear elastic simulations for void growth and remeshing of the deformed geometries. In Section 3, we provide representative examples of isotropic M-Voronoi geometries and introduce briefly the other three geometries analyzed in this work, i.e., polydisperse RSA with spherical voids, Gyroid TPMS and Spinodoids. In Section 4, we study the stiffness of the four geometries via small strain FE simulations. Section 5 deals with the numerical large strain elasto-plastic response of these geometries under uniaxial compression and simple shear loads. We conclude with Section 6. We also include appendices that describe the algorithms for remeshing and provide additional details on the meshing of the geometries.

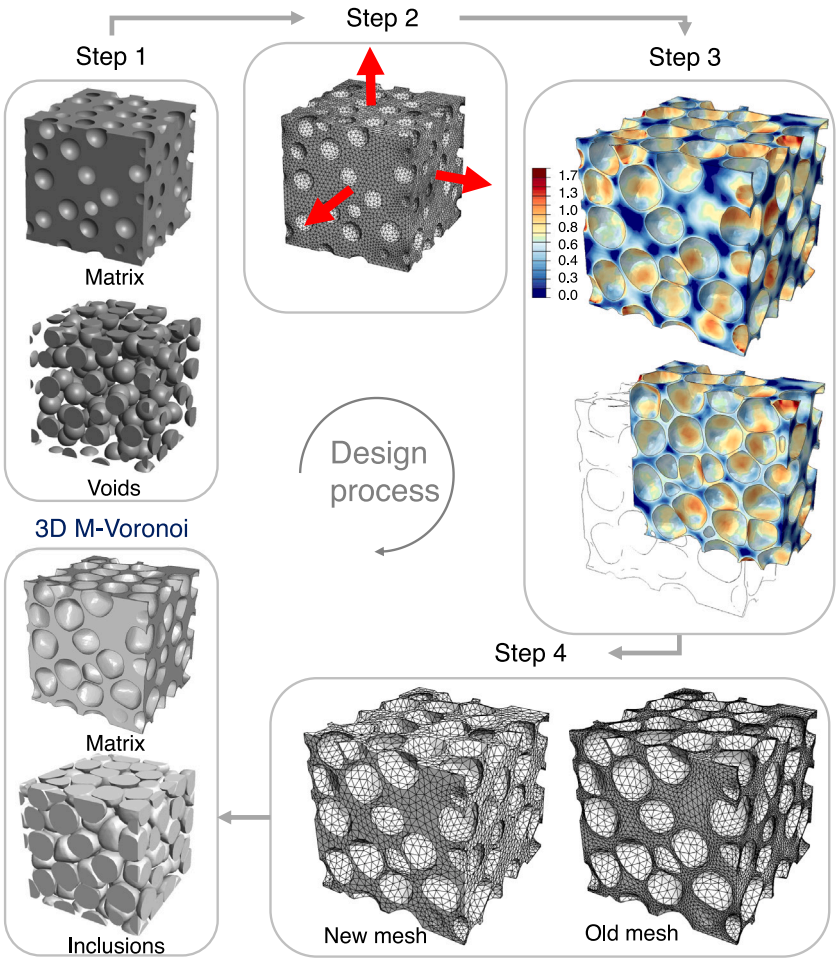

Fig. 1. Computational process for the generation of the 3D M-Voronoi material. For illustration purposes, the diagram shows the four steps required to obtain a virtual M-Voronoi geometry starting from a cubic unit-cell containing a discrete number of mono-sized spherical voids. Step 1: Random distribution of spherical voids in a cubic domain with initial relative density $\rho = 0.7$. Step 2: Application of displacement boundary conditions. Step 3: Numerical FE simulation at large strains using nonlinear elastic energy minimization and incompressible matrix behavior. The final relative density corresponds to $\rho = 0.3$. The cut image shows the inside of the deformed geometry. The color bar indicates the maximum principal logarithmic strain. Step 4: Remeshing and uniform re-scaling of the deformed geometry to the desired size. The final 3D M-Voronoi and its containing inclusions are uniformly re-scaled to the size of the initial geometry.

2. M-voronoi geometry generation

In this section, we describe the computational morphogenesis of the 3D M-Voronoi (from "Mechanically grown" Voronoi) geometries, which follows a similar procedure as the one for 2D M-Voronoi geometries presented in Hooshmand-Ahoor et al. (2022).

The procedure is divided into four main steps (see for a visual description Fig. 1).

Step 1: Random generation of spherical (or ellipsoidal) voids in a predefined volume cell (need not be unit) using the RSA method (Torquato, 2002; Anoukou et al., 2018). The distribution may be uniform (or not), periodic (or not) and the background cell may be cubic or of a different shape (see examples in Hooshmand-Ahoor et al. 2022). The size of the voids may be the same (i.e. monodisperse) or different (i.e. polydisperse). In this study, we consider a cubic, unit-cell containing initially monodisperse spherical voids randomly distributed in the cell and imposing periodicity on the lateral surfaces (although not necessary).

Step 2: Application of mechanical Dirichlet boundary conditions. Those may be periodic (or not) depending on the final design geometry target. In addition, one may relax further this boundary condition by applying a combination of Dirichlet–Neumann or only Neumann boundary conditions. The main restriction is that the total volume changes imposed on the cell must be positive, thus inducing void growth. In the present work, we apply affine Dirichlet boundary conditions, which implies that the deformed geometry will not be exactly periodic. We note that there is no particular reason in our study to maintain periodicity since the subsequent simulations are not periodic.

Step 3: Numerical simulation of the initial volume cell at finite strains and use of incompressible nonlinear elasticity for the matrix phase. This allows to transform all imposed volume changes via the external boundary conditions to pure void growth. The simulation stops when one reaches the prescribed final porosity or density desired. For very low density geometries, one needs to carry out intermediate remeshing to allow for numerical local convergence.

Step 4: Final remeshing and uniform re-scaling of the final deformed geometry to the desired size. This allows to subsequently analyze the final geometry numerically or experimentally by use of 3D-printing.

Each of these steps is further detailed in the following.

Step 1: RSA generation

The proposed void growth process begins with the construction of an initial cubic porous unit-cell. The initial void distribution and

shape affect in general the final M-Voronoi geometry. Such a study is beyond the scope of the present work and will be carried out elsewhere. In this study, we focus on initially spherical voids distributed uniformly and periodically in a unit cube. In particular, the voids are distributed following a random adsorption algorithm (RSA) (Torquato, 2002; Segurado and Llorca, 2002; Lopez-Pamies et al., 2013) and are taken to have the same size (i.e. monodisperse). The positions of the void centers are obtained randomly, and are rejected if the distance to any of the already allocated voids is less than a given limit (usually $1-5\%$ of the void diameter depending on the initial porosity as higher porosity requires decreasing this distance). For a periodic geometry, voids that lie at the edge of the unit-cell are periodically reproduced in opposite faces of the unit-cell. This step is obviously unnecessary if one is interested in non-periodic geometries or the external volume cell is not periodic (e.g. a cylinder). In order to obtain a good mesh quality, a void is rejected if the distance between its center and the edge of the RVE is in the range of 0.95–1.05% of its diameter. These conditions lead to realizations that are fairly easy to mesh with good quality finite elements. In this work, the geometry is imported in the open source `Gmsh` (Geuzaine and Remacle, 2009) software (https://gmsh.info) and meshed using quadratic, ten-node, isoparametric, tetrahedral elements. The initial porosity is user-defined and is denoted as c_0 such that the initial density is $\rho_0 = 1 - c_0$. It is important to note in passing that in principle, any void geometry may be used as a starting point for the numerical morphogenesis. For instance, one could start with Spinodoid geometries at small porosity (Soyarslan et al., 2018; Kumar et al., 2020; Maskery et al., 2017; Portela et al., 2020), periodic ones (e.g. TPMS, octahedral, etc.) or other random ones (Zerhouni et al., 2021; Neumann et al., 2020). The subsequent steps are independent of the starting geometry.

Step 2: Dirichlet boundary conditions

We choose to work in this study with periodic geometries but affine Dirichlet boundary conditions. This allows to obtain deformed cubic geometries with plane faces that can eventually be 3D-printed and tested. In addition, the use of Dirichlet boundary conditions allows for simpler control of the imposed volume change on the cubic unit-cell since it is explicitly known *ab initio* in this case. Specifically, let the deformable unit-cell occupy a volume $\mathcal{V}_0$ in the undeformed (Lagrangian) configuration with boundary $\partial\mathcal{V}_0$. The reference position vector of a material point in $\mathcal{V}_0$ is denoted with $\mathbf{X} \in \mathcal{V}_0$. The deformed position vector $\mathbf{x}(\mathbf{X})$ of any material point is related to $\mathbf{X}$ via $\mathbf{x}(\mathbf{X}) = \mathbf{X} + \mathbf{u}(\mathbf{X})$, where $\mathbf{u}(\mathbf{X})$ denotes the displacement vector of any material point. The deformation gradient is defined then as $\mathbf{F} = \partial\mathbf{x}/\partial\mathbf{X} = \mathbf{I} + \mathrm{Grad}\mathbf{u}$, where Grad denotes the gradient operator with respect to $\mathbf{X}$. We then impose

$$\mathbf{u}(\mathbf{X}) = (\mathbf{F}^{\mathrm{app}} - \mathbf{I})\,\mathbf{X} \qquad \forall \mathbf{X} \in \partial\mathcal{V}_0. \tag{1}$$

Here, the prescribed, non-symmetric, second-order tensor $\mathbf{F}^{\mathrm{app}}$ represents the average deformation gradient in the entire cell, i.e., $\mathbf{F}^{\mathrm{app}} = |\mathcal{V}_0|^{-1}\int_{\mathcal{V}_0}\mathbf{F}(\mathbf{X})\mathrm{d}\mathbf{X}$ (Hill, 1963). These boundary conditions maintain the sides of the cube straight and as a consequence, the deformed geometry loses its initial smooth periodicity.[1]

Step 3: Large strain nonlinear elastic simulations

This step involves the numerical simulation of a finite-strain, nonlinear elastic boundary value problem (BVP), whose geometry was defined in Step 1 and boundary conditions in Step 2. The solid matrix phase of the unit-cell is assumed to follow an incompressible, neo-Hookean law described formally by the Helmholtz free energy density[2]

$$W(\mathbf{F}) = \frac{\mu}{2}(\mathbf{F}\cdot\mathbf{F} - 3), \quad \text{such that} \quad C(\mathbf{F}) = \det\mathbf{F} - 1 = 0. \tag{2}$$

Here, μ denotes the shear modulus, which, for the purposes of this study, may be set equal to unity, while the incompressibility constraint $C(\mathbf{F})$ needs to be imposed everywhere in the matrix phase. The pointwise displacement $\mathbf{u}$ and pressure p (Lagrange multiplier associated with the incompressibility constraint) are then obtained by optimizing the nonlinear elastic energy everywhere in the solid matrix phase (Fu and Ogden, 2001)

$$\{\mathbf{u}, p\} = \arg\left\{\min_{\mathbf{u}^*\in\mathcal{K}(\mathbf{F}^{\mathrm{app}})}\max_{p}^{*}\int_{\mathcal{V}_0} W(\mathbf{F}(\mathbf{u}^*)) + pC(\mathbf{F}(\mathbf{u}^*))\mathrm{d}\mathbf{X}\right\}, \tag{3}$$

where $\mathcal{K}(\mathbf{F}^{\mathrm{app}}) = \{\mathbf{u} : \text{regular}, \mathbf{u} = (\mathbf{F}^{\mathrm{app}} - \mathbf{I})\,\mathbf{X}, \quad \forall\mathbf{X} \in \partial\mathcal{V}_0\}$. The above BVP is then solved by the finite element (FE) method with the commercial software ABAQUS (Dassault Systems). For this, quadratic 10-node, three-dimensional (3D) hybrid elements (`C3D10H`) are used to deal with incompressibility. The void phase has no energy density and is therefore left un-meshed with traction-free boundaries. Despite the incompressibility of the solid phase, the unit-cell is porous and thus compressible. Therefore, by prescribing $\det\mathbf{F}^{\mathrm{app}} > 1$, the volume of the unit-cell increases. This is readily achieved via void growth and local shearing of the matrix phase. Given the incompressibility of the solid phase, mass conservation and the prescribed boundary conditions, the following kinematic relation may be derived between the initial relative density ρ_0 (or porosity c_0) and final relative density ρ (or final porosity c) of the unit-cell

$$\rho = \frac{\rho_0}{\det\mathbf{F}^{\mathrm{app}}} \qquad \text{or} \qquad c = 1 - \frac{1 - c_0}{\det\mathbf{F}^{\mathrm{app}}}. \tag{4}$$

This relation implies that the final relative density (or porosity) of the unit-cell can be exactly controlled by the value of $\det\mathbf{F}^{\mathrm{app}}$ that needs to be applied.

In the context of Dirichlet-only boundary conditions, the deformed volume of the unit-cell, $\mathcal{V}$, is entirely defined in terms of the prescribed deformation gradient $\mathbf{F}^{\mathrm{app}}$ from the purely kinematic relation $\mathcal{V} = \det\mathbf{F}^{\mathrm{app}}\,\mathcal{V}_0$. If mixed Dirichlet–Neumann (or only Neumann) boundary conditions were applied, still expression (4) is valid with $\mathbf{F}^{\mathrm{app}}$ replaced by the average deformation gradient in the unit-cell. Nevertheless, in this latter case, the average deformation gradient is not explicitly known but is the solution to the nonlinear finite deformation problem (3).

Finally, if a compressible matrix phase is used instead, part of the imposed dilation will be absorbed by the matrix phase. The evaluation of this proportion is not analytical and thus requires a continuous recording of the current porosity by post-processing to reach the desired value. Instead, for a quasi-incompressible matrix, the results are expected to be fairly close to the purely incompressible case depending on the value of the bulk modulus that will be used.

[1] Use of periodic conditions is obviously possible by simply adding a periodic displacement field (see Michel et al. (1999) and Mbiakop et al. (2015)). This, however, would lead to wavy fluctuating deformation of the cube sides. As we will see in the next section, our goal is to simulate a boundary value problem that is potentially realizable via 3D-printing (see for instance Hooshmand-Ahoor et al. (2022)) and pertains to a pragmatic realization of the geometry at hand. For this reason, we do not impose periodic boundary conditions. The proposed affine boundary conditions maintain some form of "periodicity" since they impose that the cube faces remain flat throughout the process.

[2] We note that other forms of energy functions may be prescribed. Nevertheless, due to the large strains, the simple neo-Hookean law has shown better numerical convergence. By contrast, the use of elasto-plasticity would lead to strain localization and highly heterogeneous void growth and thus is not recommended for such geometry construction.

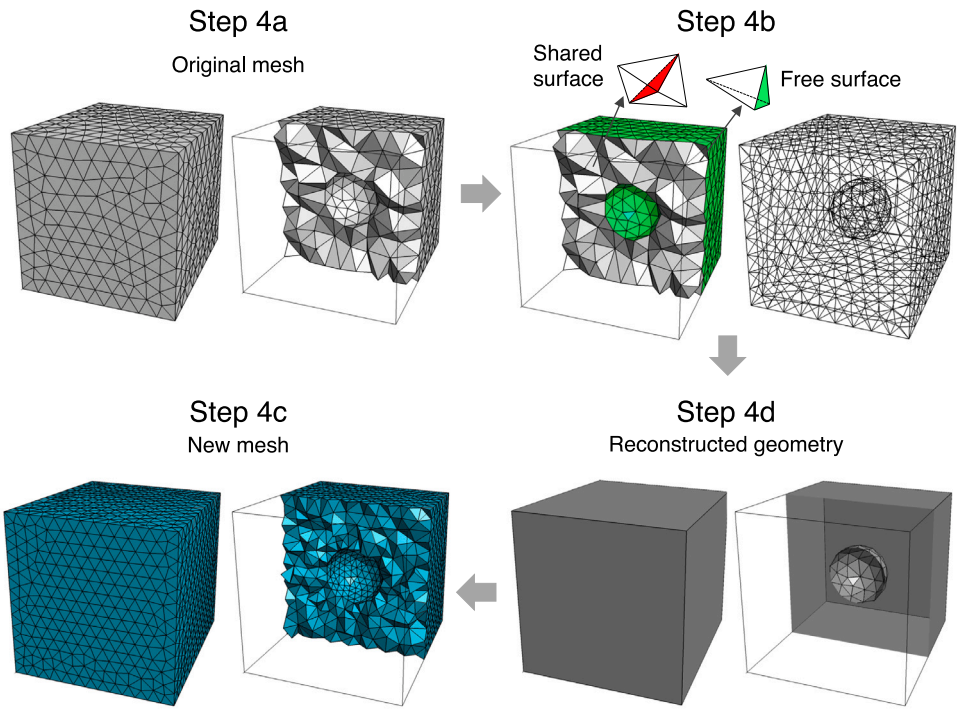

Fig. 2. The developed remeshing algorithm for an orphan mesh based on geometry reconstruction. For illustration purposes, a simple 3D orphan mesh containing a spherical void is used. The diagram shows the four steps required to remesh an orphan mesh. Step 4a: Reading the nodes and elements of the orphan mesh. Step 4b: Finding the free surfaces of the elements. The green color corresponds to accepted free surfaces, whereas the red regions are rejected shared surfaces. Step 4c: Constructing the geometry of the orphan mesh. Step 4d: Remeshing the new mesh with an arbitrary mesh algorithm.

Step 4: Geometry reconstruction and remeshing algorithm

The finite strain simulations in the previous step often lead to severe mesh distortion and eventual termination of the numerical simulations before reaching the desired porosity. Even if one reaches the prescribed final porosity, the resulting mesh is extremely distorted to perform any subsequent simulation or export the geometry for 3D-printing. In both scenarios, a remeshing is required either at an intermediate strain level to allow for the simulation to continue further or at the final state. Recently, a method was used in Luo et al. (2023) to perform such remeshing in three-dimensions based on the original work of Hooshmand-Ahoor et al. (2022) in two-dimensions. That method was only described briefly in that work since the focus was different. Here, we provide more details on the approach. In particular, the proposed remeshing approach has the following non-trivial properties:

- produces the geometry of any orphan mesh,
- preserves the deformed discretized geometry without any approximation (up to the FE discretization accuracy),
- can identify regions with no elements i.e. void domains,
- can identify different phases, which is relevant for multi-phase materials,
- can deal with both two- and three-dimensional geometries,
- can deal with different simplicial and hexahedral element types.

In the following, we describe the philosophy of the proposed remeshing approach, which is divided into four substeps and is also summarized in Fig. 2. The detailed set of algorithms is given in Appendix A. For illustrative purposes, we consider a simpler 3D geometry containing a single spherical void in the middle of the cube.

Step 4a *: Import the orphan mesh and read the nodes and elements.* We first read the node and element data of the orphan mesh and store them in corresponding matrices. We consider that the orphan mesh contains n nodes and each node i contains three coordinate components x_i, y_i, z_i in three dimensions. We define a matrix $\mathbb{N}_{n\times 3}$, containing the information of all nodes such that $\text{row}_i(\mathbb{N}) = (x_i, y_i, z_i)$. Similarly, we define a matrix $\mathbb{M}_{m\times h}$ to store the information of the elements. In this matrix, m is the number of elements and h denotes the number of nodes for each element, which may vary depending on the type and order of the element. We have considered the most common element types corresponding to tetrahedral and hexahedral elements with linear or quadratic element orders, i.e., $h = 4, 8, 10, 20$. One may extend this method to other element types such as a triangular prism or higher order quadrature. Step 4a in Fig. 2 represents an orphan volume mesh of a matrix containing one spherical void, while the right side image shows a cut view of the mesh.

Step 4b *: Find the free surfaces of the elements.* The resulting geometry from the remeshing algorithm will be written in `Gmsh` format, which is an open source software. It may be further converted to other CAD formats if required. `Gmsh` allows building a complex 3D closed volume by connecting a series of planes, which are the surface planes that make the exterior boundary of the volume. The free surfaces of an orphan mesh belong only to one element. In turn, a shared surface of an element is shared by two elements simultaneously. The left image of the Step 4b in Fig. 2 displays the identification process of the free surfaces. The green surfaces correspond to the free surfaces of the individual elements and the red ones to the shared ones. The right image of Step 4b shows all identified free points (nodes) and element surfaces of the orphan mesh. These surfaces are used to construct the geometry in the next step. The algorithm for finding the free surfaces of an orphan mesh is described in Algorithm 1 in Appendix A.

In a nutshell, the surfaces that are not in common between two different elements are identified and stored as free surfaces. The process consists of two main loops that compare the nodes at each surface of an element with all other elements. We consider that each surface of an element contains 3 or 4 nodes for the tetrahedral or hexahedral element type. In the case of quadratic elements, the middle nodes are identified according to the corner nodes. To speed up the loops, we define a matrix that contains the elements connected to each node in order to limit the search over all elements, which results in a significant

improvement in the speed of the algorithm. The free surfaces are stored in the matrix $\mathbb{S}_{f\times r}$, where f denotes the total number of free surfaces and $r = 3, 4, 6, 8$ corresponds to the number of nodes on every side of elements and will vary depending on the element type and order. It is noted that the type and order of the elements are determined as input by the user.

Step 4c *: Construct the 3D geometry by the free element sides.* The identified free surfaces from Step 4b are then connected in order to construct the closed volumes of the 3D geometry. The geometry entities are built in a bottom-up manner (first points, then curves, surfaces, and finally volumes) with the built-in OpenCASCADE kernel of the geometry module in the `Gmsh`. Specifically, we denote every identified free surface by $s_i = \mathbb{S}(i, 1 : r)$, which is surrounded by more than two free surfaces. Initially, the algorithm starts with the first free surface $s_1 \in \{s_1, s_2, \dots, s_f\}$ and then finds the second free surface connected to it, which is determined by the node in common between the two neighboring surfaces. The distinction between different closed volumes $v_i \in \{v_1, v_2, \dots, v_N\}$ of the geometry is performed by checking whether all remaining surfaces have no nodes in common with the current volume. The process terminates when all free surfaces have been taken into account and N volumes are reconstructed.

Identifying multiple surface-loops/volumes implies that the orphan mesh consists of a multi-phase material (i.e. there are either voids or particles or a combination of both).[3] Whenever required, we use the Boolean operations available in the `Gmsh` Open-CASCADE kernel to cut out the volume of the voids from the matrix or create a conformal mesh at the particle-matrix interface.

It is worth mentioning that the proposed method requires all data from the previous geometrical entities and thus can become extremely time consuming. In order to speed up the process, we have limited the search over all elements by looping over the defined matrix in Step 4b, which contains the elements connected to each node. Therefore, the construction process even with extremely complex geometry does not exceed a few seconds. This algorithm is described in Algorithm 2 in Appendix A.

Step 4d *: Export the geometry, rescale and remesh.* The constructed geometry that is written in `Gmsh geo` format can be subsequently converted into any CAD version or meshed with any desired method. Specifically, in contrast to other existing remeshing methods, having the geometry gives full control over the output mesh type. For example, both the final geometry and the new mesh can be uniformly (or non-uniformly) re-scaled to a specific size by multiplying all nodal coordinates by a fixed set of three numbers along three different directions. In our study, the new mesh is created with `Gmsh` software and is exported as an Abaqus input file (.inp) for simulations with different element types and orders.

The remeshing approach described in detail here has already been used in Luo et al. (2023) to carry out large strain simulations of particle reinforced composites where remeshing and stress mapping were necessary. In turn, the two-dimensional variant of the approach has been used in Hooshmand-Ahoor et al. (2022) to export, 3D-print and experimentally test M-Voronoi porous materials.

3. Examples of M-Voronoi and other random and periodic geometries

We apply the previously discussed M-Voronoi generation process to obtain geometries of a wide range of porosities in a cubic domain. It is important to note here that such non-spherical void shapes have already been presented in the earlier works of Moraleda et al. (2007) and Michel et al. (2007), albeit with a scope of estimating the homogenization response of such RSA porous materials at finite strains. Furthermore, we recall again that the geometry choice for unit-cells is not limited to a cubic shape, but this is beyond the scope of the present study (see Hooshmand-Ahoor et al. (2022) for relevant examples of non-standard cells and loads).

In order to keep this study of readable size and since our interest lies in comparing the M-Voronoi geometries with existing isotropic and cubic ones, we specialize to isotropic purely hydrostatic deformation gradients, i.e., $\mathbf{F}^{\text{app}} = \text{diag}(\lambda^{\text{app}}, \lambda^{\text{app}}, \lambda^{\text{app}})$ with $\lambda^{\text{app}} > 1$ such that $\det \mathbf{F}^{\text{app}} = (\lambda^{\text{app}})^3 > 1$.

In Fig. 3, we start with 110 initially spherical voids and initial relative density $\rho_0 = 0.7$ ($c_0 = 0.3$). The spherical voids progressively grow into smooth polyhedral-type shapes, as is visually evident in the cross-sectional view of the cells at the bottom of Fig. 3. This complex geometry of the voids arises from the intricate interplay between the disordered void distributions and the non-linear large deformations of the surrounding matrix. This leads to Voronoi-type inclusion shapes that are convex and non-quadratic. Furthermore, due to the random distance between the centers of the initial spherical voids, the deformed intervoid ligaments have a random variation in thickness. As one increases the applied λ^{app} to reach higher porosities the intervoid ligament thickness becomes more uniform (see for instance the cell corresponding to $\rho_0 = 0.01$, which is an extremely low density closed-cell random foam).

More importantly, it is evident that the proposed M-Voronoi geometries are realizable at solid densities spanning the full spectrum from 1 to very low (e.g., 0.01) as represented in Fig. 3. In order to obtain very low relative densities $\rho \leq 0.2$, it is required to perform intermediate remeshing to assist the simulations to reach the low targeted relative density. In this example, in order to achieve the M-Voronoi with relative densities $\rho = 0.2, 0.1$, we have performed a remeshing of the M-Voronoi geometry with $\rho = 0.3$ and resumed the process without mapping the stress fields. Since the interest here is in the final geometry and not the stress distributions, this strategy is acceptable and less time consuming. Using stress mapping is of course possible (see recent work of Luo et al. (2023)). Nevertheless, we have found that the resulting geometry changes only by little and given that it is random with little dispersion in properties (as we will show in the following sections) such an additional stress mapping requirement is not necessary.

For even lower relative densities i.e., $\rho = 0.05, 0.01$ a second remeshing is required of M-Voronoi geometries with $\rho = 0.1$. As a result of the limitations of the remeshing algorithm for severely distorted quadratic elements (see Appendix B), the new mesh is generated using linear tetrahedral elements, `C3D4H`, so that the final geometry can be constructed accurately after remeshing in low densities. Again, the very accurate resolution of the stress fields in these extreme cases is of secondary importance compared to the quality of the grown geometry.

The M-Voronoi geometries analyzed in this study are compared with existing geometries in the literature in order to gain insight into their corresponding mechanical properties (see Fig. 4). The possibilities of other comparison geometries that may be found in the literature are countless and impossible to cover in one study. We choose to work with three well-known geometries that were found in previous studies to be fairly isotropic or at least cubic and provide rather stiff responses as compared to other periodic or random geometries. These geometries are

- the Gyroid geometry (Fig. 4b) which is a type of Triply Periodic Minimum Surface (TPMS) geometry introduced by Schoen (1970). It has been investigated extensively in different studies and it was found to be easy to design and rather stiff in terms of mechanical properties. Since it is periodic in nature it exhibits *a priori* a cubic symmetry and is not isotropic,

[3] The number and type of phases can be assessed by the number of element sets in the orphan mesh. In particular, when the material is porous, there is only one element set for the matrix phase.

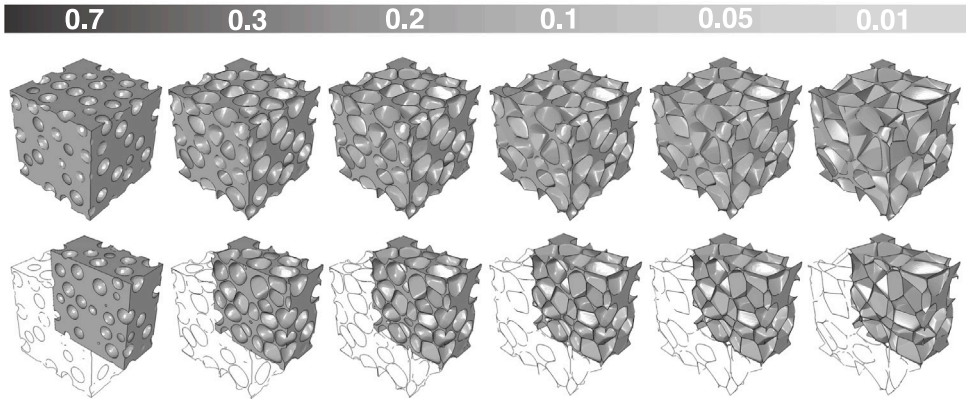

Fig. 3. 3D M-Voronoi obtained by using RSA geometry with initial relative density $\rho_0 = 0.7$ (The first geometry). The color bar indicates the final relative density ρ and the bottom images represent the void shapes inside of the geometry. The densities $\rho \leq 0.2$ are obtained by using the corresponding $\rho = 0.3$ as an initial geometry after remeshing it.

- the RSA with spherical voids (Fig. 4c) (Segurado and Llorca, 2002; Lopez-Pamies et al., 2013; Anoukou et al., 2018), which was shown to lie very close to the Hashin–Shtrikman bounds in linear elasticity experimentally and numerically (Zerhouni et al., 2019; Tarantino et al., 2019),
- the Spinodoid geometry (Fig. 4d) introduced recently by Soyarslan et al. (2018),Hsieh et al. (2019) and Kumar et al. (2020) which is closely related to the well-known thresholded Gaussian Random Field (GRF) approach (Roberts and Garboczi, 2001; Zerhouni et al., 2021). Such a geometry was found to be promising in the inverse design of isotropic and anisotropic porous materials (Kumar et al., 2020).

The features of each geometry are discussed in more detail below.

The Gyroid TPMS geometry (Fig. 4b) is constructed by approximating a surface in the Euclidean space $\mathbb{R}^3$ via the equation: $\sin(x)\cos(y) + \sin(y)\cos(z) + \sin(z)\cos(x) = 0$. Specifically, we employ the TPMS Designer, developed by Jones et al. (2021), which is a MATLAB-based software for designing cellular structures. Nevertheless, the Gyroid surface generated therein does not have the necessary mesh quality for numerical simulations at large strains. To enhance the mesh quality, we use the open source software MeshLab (Cignoni et al., 2008). For large strain numerical simulations, we also transform the improved surface mesh into a volume mesh using `Gmsh`. Despite their inherent periodicity, the Gyroid geometries have non-uniform ligament thickness and can span relative densities from 0.1 to 1. Below $\rho = 0.1$, we observe the occurrence of disconnected regions and thus we cannot proceed to lower densities with this approach. Furthermore, the complex curvature present in such Gyroid geometries poses significant challenges in both meshing and manufacturing processes. It is important to mention that although Gyroid geometries are stiffer than most of the periodic structures, their response exhibits cubic symmetry (Bonatti and Mohr, 2019).

The random sequential adsorption (RSA) method (Lopez-Pamies et al., 2013) leads to geometries with randomly distributed spherical voids of varying sizes (i.e. polydisperse) or single size (i.e., monodisperse) in a cubic domain (Fig. 4c). The RSA geometries have random features similar to the M-Voronoi ones such as random ligament thickness. They allow for a complete control of the void shapes and thus are easier to use to cover a wide range of behaviors from isotropic to anisotropic and from stiff to soft ones. M-Voronoi, by construction, are seamless descendants of the RSA geometries as explained before and exhibit almost identical constitutive responses at small and moderate porosities (i.e. $c \leq 0.4$). By contrast, it is substantially more difficult to generate representative RSA geometries at low relative densities ($\rho < 0.3$) as already discussed in Tarantino et al. (2019), since they require an extremely large range of void sizes in that case. This implies that numerical simulation and experimental realization become prohibitive at such large porosities.

The random Spinodoid solid geometries (Fig. 4d) are obtained through spinodal phase separation by Gaussian random field (GRF). Despite the random features of Spinodoid geometries and their ability to offer tailored isotropic and anisotropic responses (Soyarslan et al., 2018; Kumar et al., 2020), they can only cover a limited relative density range between 0.7 and 0.2 (Maskery et al., 2017), unless a shell type process is used (Hsieh et al., 2019). More importantly, it appears to be extremely challenging to create a volume mesh on Spinodoid geometries, mainly due to their complex and highly curved patterns. In fact, there exist numerous regions where the local curvature is extremely high leading evidently to stress concentrations and difficulty in meshing. These features obviously become (as we will see in the following) more critical at large strains than at small ones. In this work, Spinodoid geometries are created by use of the Gibbon Matlab Toolbox (see more in Kumar et al. (2020)). The volume mesh generation for Spinodoid geometries has to undergo a complex and time consuming process primarily using Meshlab software to ensure sufficient mesh quality for small and large strain simulations. It is also worth mentioning that the Kumar et al. (2020) process does not produce by default smooth interfaces between the voids and the matrix, thus making those materials more prone to deformation localization, especially in the present context of elasto-plasticity.

We close by noting that the proposed M-Voronoi geometries are realizable at a full density range and encompass various random characteristics, such as void shape, size, distribution, and ligament thickness. Furthermore, with the assistance of the developed remeshing algorithm in Appendix A, the volume mesh generation process for M-Voronoi geometries is fast, efficient and grants precise control over the resulting mesh quality at least up to relatively low densities ($\rho \geq 0.07$). At extremely low densities, i.e. $\rho < 0.05$, the volume meshes become extremely fine, and thus not suitable for large deformations, but remain fairly accurate for 3D-printing. For $\rho \leq 0.05$, the M-Voronoi resemble closely the standard Voronoi constructions (see Hooshmand-Ahoor et al. 2022) both in geometry and constitutive response. For the latter, it is straightforward to use shell elements to analyze the very low relative density regime.

In the following sections, we will examine the mechanical behavior of the M-Voronoi geometries at both small and large strains over a wide relative density range and compare the corresponding results with Gyroid, RSA and Spinodoid geometries.

4. Elastic stiffness response at small strains

In this section, we study the macroscopic linear elastic properties of M-Voronoi, Gyroid, RSA and Spinodoid geometries over their attainable range of relative densities through numerical simulations. Given that the Spinodoids are not periodic and the fact that we are interested in the apparent response of the designed geometries, we will focus in

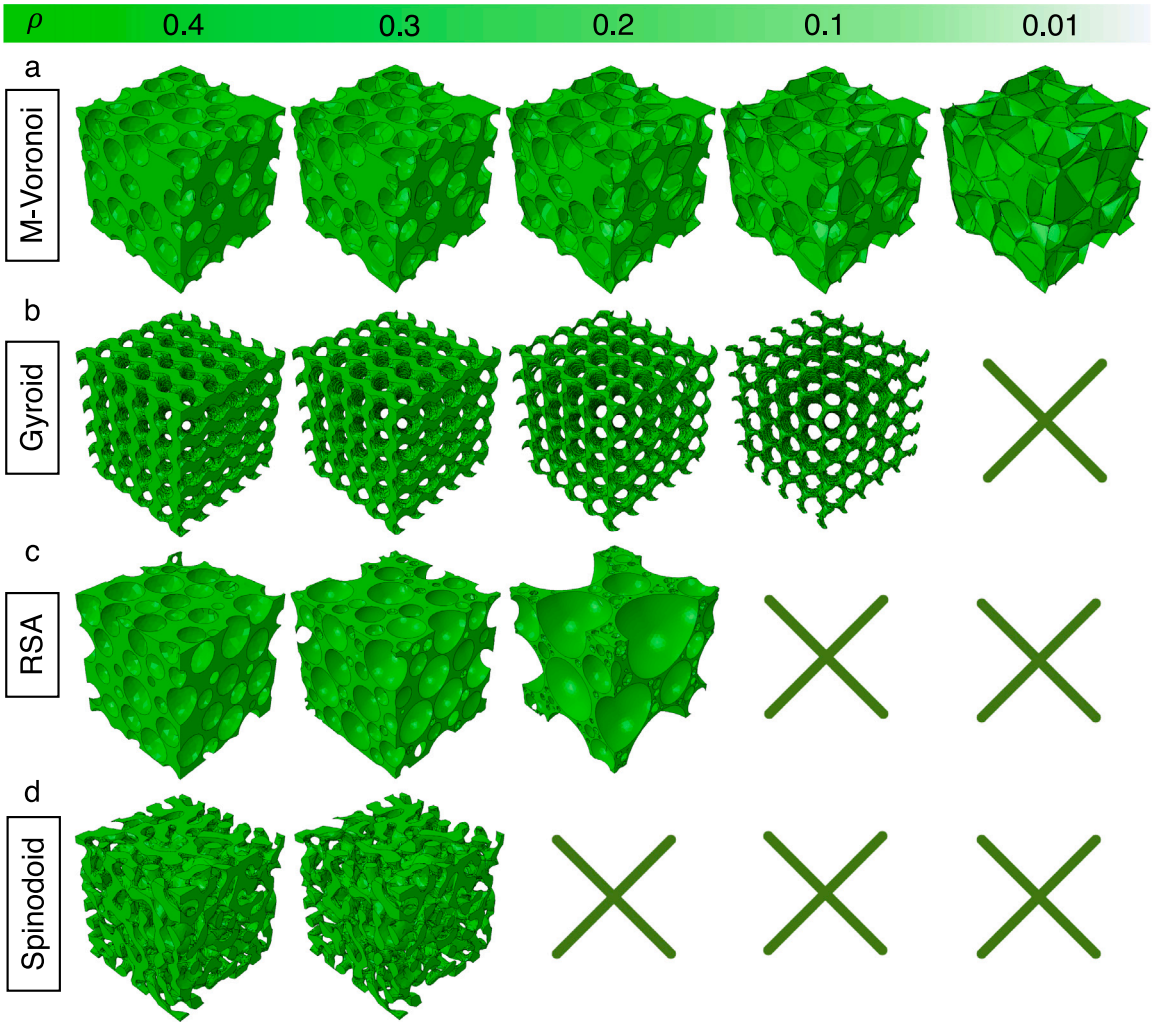

Fig. 4. (a) M-Voronoi with 110 voids obtained by using an RSA geometry with initial relative density $\rho_0 = 0.7$. (b) Gyroid lattices with $5 \times 5 \times 5$ unit-cells. (c) Polydisperse RSA geometries with various sphere sizes. (d) Spinodoid geometries obtained through spinodal phase separation by Gaussian random field (GRF). The color bar indicates the relative density ρ of the geometries. The cross shows the unrealizable geometries.

the next two sections on non-periodic boundary conditions. The reason for such a choice is related to the recent works of Zerhouni et al. (2019),Tarantino et al. (2019) and Hooshmand-Ahoor et al. (2022), where the realization of these geometries via 3D-printing and experimental testing was shown to be possible. In particular, it was shown therein that periodic conditions by construction lead rapidly (i.e. with the use of less number of voids) to representative material response. Because of this fast convergence, they provide no practical information on the size of the RVE that is required for experimental `material` representativity. For this reason, having in mind the potential experimental realization of such materials, we focus on non-periodic, realistic boundary conditions.

We obtain the macroscopic (apparent) elastic moduli for random porous geometries through linear elastic finite element (FE) simulations performed on unit-cells using Abaqus/Standard finite element software and following the approach of Kanit et al. (2003). Simulations are performed using standard linear 8-node hexahedral elements (C3D8 in Abaqus). Examples of such meshes and the procedure for obtaining them are discussed in Appendix C. The matrix phase is modeled as purely isotropic linear elastic without any plasticity, while the void phase is left unmeshed. The unit-cell is subjected to a kinematically uniform boundary conditions (KUBC) (Michel et al., 1999; Mbiakop et al., 2015) defined such that the displacement field $\mathbf{u}(\mathbf{x})$ at point $\mathbf{x} = \mathbf{X}$ (at small strains) in the microstructure is given by

$$\mathbf{u}(\mathbf{x}) = \boldsymbol{\varepsilon}^{\text{app}}\,\mathbf{x}, \tag{5}$$

where $\boldsymbol{\varepsilon}^{\text{app}}$ is a constant second-order symmetric tensor. Given that the number of voids is sufficiently large, one may consider the response representative at least in the context of linear elasticity as shown recently by Zerhouni et al. (2019).

We compute the homogenized fourth-order elastic stiffness tensor $\mathbf{C}$ from the average stress and strain fields through the constitutive equation (Hill, 1963)

$$\langle \boldsymbol{\sigma}(\mathbf{x}) \rangle = \mathbf{C}\,\langle \boldsymbol{\varepsilon}(\mathbf{x}) \rangle, \tag{6}$$

where $\langle \cdot \rangle$ denotes the volume average of the enclosed quantity. It is readily obtained by use of the affine conditions in (5) that the average strain in the cubic cell is equal to the externally applied one, i.e., $\langle \boldsymbol{\varepsilon}(\mathbf{x}) \rangle = \boldsymbol{\varepsilon}^{\text{app}}$. The macroscopic elastic stiffness tensor $\mathbf{C}$ is computed by running six independent calculations (taking into account the symmetry of the applied strain), where a uniform macroscopic strain is applied along a specific direction, i.e. $\varepsilon_{ij}^{\text{app}}$ with $i, j = 1, 2, 3$ (no sum on i, j). Due to the finite number of voids, the tensor $\mathbf{C}$ is not exactly isotropic. In order to extract meaningful quantities and evaluate its deviation from isotropy, we define an isotropic stiffness tensor, denoted by $\mathbf{C}^{iso}$, which is calculated by the projection of $\mathbf{C}$ along the fourth order hydrostatic and deviatoric space by use of the tensors

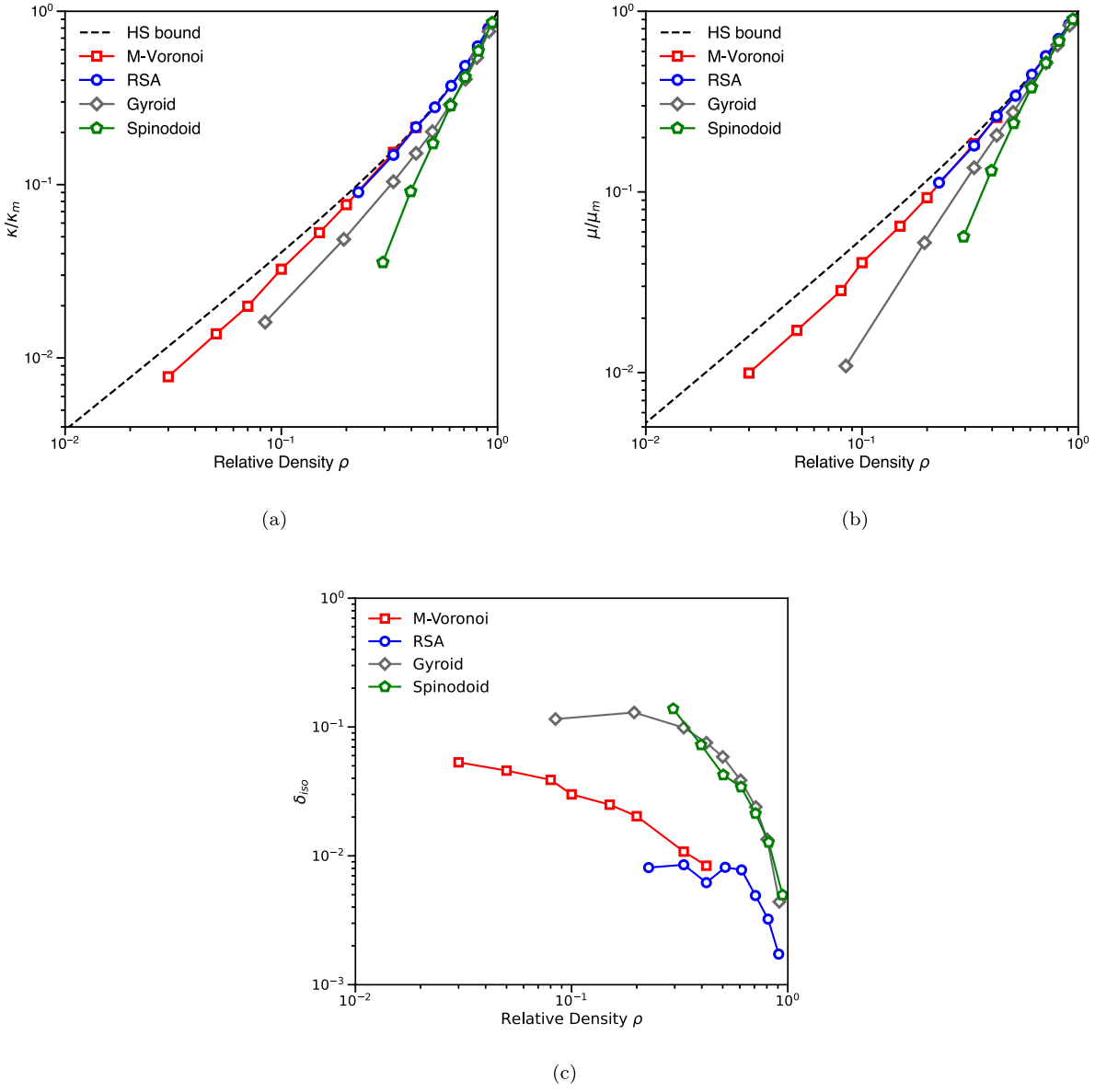

Fig. 5. (a) Normalized bulk modulus κ/κ_m and (b) shear modulus μ/μ_m as a function of relative density ρ obtained by FE simulations together with the Hashin–Shtrikman bounds (dashed lines) that are included for comparison, (c) Deviation from isotropy δ_{iso} for different geometries and various values of relative density ρ. κ_m and μ_m denote the bulk and shear moduli of the matrix phase and a matrix Poisson ratio $\nu_m = 0.3$ is used in all simulations.

J and **K**, respectively,[4] as

$$\mathbf{C}^{iso} = 3\kappa\,\mathbf{J} + 2\mu\,\mathbf{K}, \quad \kappa = \frac{1}{3}\mathbf{C}\cdot\mathbf{J} = \frac{C_{iijj}}{9}, \quad \mu = \frac{1}{10}\mathbf{C}\cdot\mathbf{K} = \frac{3C_{ijij} - 9\kappa}{10}. \tag{7}$$

Here, κ and μ correspond to the apparent projected bulk and shear moduli, respectively, shown in Fig. 5a,b. The deviation from isotropy is, in turn, defined in terms of a scalar parameter δ_{iso}, evaluated as

$$\delta_{iso} = \frac{\|\mathbf{C} - \mathbf{C}^{iso}\|_F}{\|\mathbf{C}\|_F}. \tag{8}$$

Here, $\|\mathbf{A}\|_F = \sqrt{\mathrm{Tr}(\mathbf{A}\cdot\mathbf{A}^T)}$, is the Frobenius norm of the tensor **A**. The case of $\delta_{iso} = 0$ corresponds to exact isotropy. This measure is more complete than the Zener measure since it addresses all shear components diagonal and off-diagonal. It is evident that for a proper interpretation of the following results, one should analyze all three quantities simultaneously, i.e., μ, κ and δ_{iso}. The numerically-obtained apparent projected elastic properties of the porous geometries are also compared with the Hashin–Shtrikman (HS) theoretical bounds for the bulk and/or shear modulus (Hashin and Shtrikman, 1963). In Fig. 5a,b, we observe the results from the FE simulations of M-Voronoi, RSA, Gyroid and Spinodoid geometries as a function of the relative density $\rho = 1 - c$ (c denoting the porosity). Here, κ/κ_m and μ/μ_m correspond to the normalized apparent bulk and shear moduli, respectively. In turn, κ_m and μ_m denote the bulk and shear moduli of the matrix phase. In all simulations, we have used a Poisson ratio $\nu_m = 0.3$ for the matrix phase. The effective bulk and shear modulus of the M-Voronoi and RSA geometries for relative densities up to 0.2 are almost identical and lie very close to the Hashin–Shtrikman (HS) bounds. This similarity arises primarily from the shared microstructure characteristics of these two geometries, i.e., the random void and intervoid ligament sizes. However, contrary to the RSA geometries, which have a limited relative density range, M-Voronoi geometries can be simulated in the case of

[4] The hydrostatic and deviatoric projection tensors are defined by $J_{ijkl} = (1/3)\delta_{ij}\delta_{kl}$ and $\mathbf{K} = \mathbf{I} - \mathbf{J}$, respectively. **I** is the identity fourth-order tensor such that $I_{ijkl} = (1/2)(\delta_{ik}\delta_{jl} + \delta_{il}\delta_{jk})$, while δ_{ij}(with $i = 1, 2, 3$) is the identity second-order tensor. We note that **J** and **K** follow the relations $\mathbf{J}\cdot\mathbf{J} = \mathbf{J}$, $\mathbf{K}\cdot\mathbf{K} = \mathbf{K}$, and $\mathbf{J}\cdot\mathbf{K} = \mathbf{K}\cdot\mathbf{J} = \mathbf{0}$.

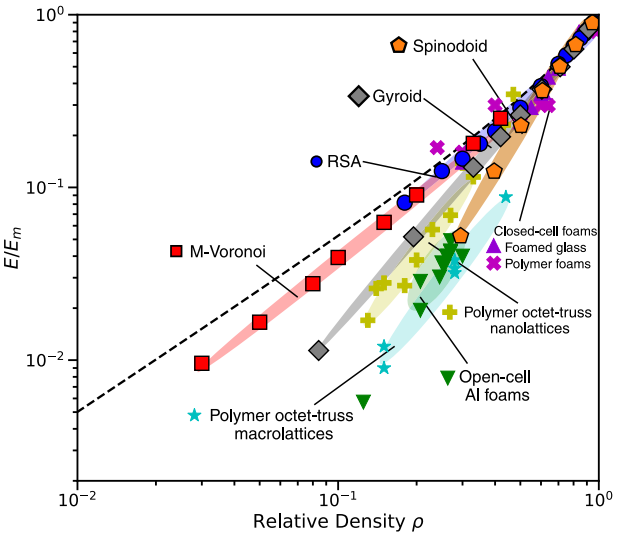

Fig. 6. A property space map of Young's modulus versus relative density ρ comparing the present geometries of M-Voronoi, RSA, Gyroid, and Spinodoid to other closed- and open-cell foams of similar density and to nano- and macro-lattices.

small strain elasticity up to relative densities as low as $\rho = 0.03$. The effective properties of both Gyroid and Spinodoid geometries exhibit substantial deviations from the HS bounds when relative densities fall below 0.5. Notably, the deviation is more pronounced in the case of Spinodoid solid geometries, for which we have been able to simulate only up to relative densities $\rho = 0.3$.

In summary, M-Voronoi and RSA geometries exhibit the stiffest response compared to the Gyroid and Spindoid geometries. Given the simplicity of the generation of RSA geometries, at relative densities $\rho > 0.3$, they are a promising option among the studied geometries. At lower relative densities, one may use the M-Voronoi geometry which shows very promising properties, despite the complexity of its generation.

The previous elastic results should be interpreted in direct connection with the deviation from isotropy δ_{iso}, shown in Fig. 5c. We observe that in RSA geometries, the numerical deviation from isotropy is found to be less than 0.01 for $\rho \in [0.2, 1]$. The deviation from isotropy in M-Voronoi geometries on the other hand, develops gradually, reaching a value of ~ 0.06 at $\rho = 0.03$. The δ_{iso} values of Gyroid and Spinodoid geometries are similar and are generally greater than those for M-Voronoi and RSA geometries at equivalent corresponding densities. While that is expected for the Gyroid geometries, which are naturally cubic, the strong deviation of anisotropy for the Spinodoids implies that they need a substantially smaller wavelength to reach isotropy. This makes their realization and simulation extremely difficult with standard FE. Instead, one could use FFT grids as an alternative. Note, however, that FFT solvers cannot handle the large strain compressive simulations of the following section. These observations are consistent with recent studies on the very similar thresholded Gaussian Random Field geometries (Zerhouni et al., 2021).

Fig. 6 compares the apparent Young's modulus obtained in the present study with available data in the literature for other porous materials and fully stochastic foams manufactured using conventional processes like foaming and replication (Tarantino et al., 2019). It can be observed that the M-Voronoi geometries of this work exhibit the stiffest response among all the shown data and lie very close to the HS bounds (denoted with a dashed line) over a very wide density range (up to 0.03). Moreover, we observe that both M-Voronoi and RSA exhibit a rather nonlinear response with ρ and thus any scaling law would have had a small range of validity and thus no such analysis is carried out here.

5. Elasto-plastic response at large strains

In this section, we assess the mechanical properties of 3D M-Voronoi geometries at large deformations and for elastic ideally-plastic matrices.

The interest in this study is in the large strain response of the previously-described geometries and in particular for fairly low densities. We focus on two such loading conditions: uniaxial compression and simple shear. The first is of practical importance and the second allows us to probe the large strain diagonal anisotropy that may develop as compared to the corresponding one in compression.

Due to the finite strains and extensive *random* contact between void surfaces, the only possible option is the use of an explicit solver instead of an implicit one. In the present study, we use the Abaqus/Explicit solver with the `*NLGEOM` option activated and sufficiently small rates and time increments to preserve quasi-static conditions and numerical convergence. We consider an elastic ideally-plastic matrix phase with a fixed yield stress σ_y, Young's modulus $E_m = 1000\sigma_y$ and Poisson's ratio $\nu = 0.3$. All results are readily normalized with the matrix yield stress by considering a value $\sigma_y = 1$.

An extensive study of the effect of element type (not shown here for brevity) has shown that brick hexahedral, reduced integration, linear elements (`C3D8R`) are the best candidates for elasto-plastic simulations leading to a very good numerical convergence and acceptable cpu computation time. The three-dimensional mesh in all geometries is created with `Gmsh` software using the hexahedra subdivision algorithm (see Appendix C). The computation time for a hexahedral element-type mesh with 9×10^5 nodes corresponds to approximately 100 h when running on 40 cores in parallel. This requires in general extremely large amounts of memory and thus the possibility of restarting the simulations is primordial. To achieve this, extensive use of the option `OVERLAY`, which stores the data in the most recent increment and removes the previously stored data is done to minimize memory usage given the very large domain sizes in the considered geometries. The simulation is then resumed by the use of the `RECOVER` option.

5.1. Results: uniaxial compression

This section presents the results obtained for the M-Voronoi, RSA, Gyroid and Spinodoid geometries when subjected to large strain uniaxial compression loading. In particular, we carry out the simulation by applying a displacement normal to one of the cube surfaces, while blocking the other two tangential components. At the opposite surface, we apply clamped boundary conditions. The remaining side surfaces of the cube are left traction-free. Such a load mimics rather closely realistic conditions in the laboratory and thus experimental data in the literature. Instead, one could apply a pure uniaxial compression. The differences between those two loading conditions are fairly small for such high porosity foams.

All stress measures in this section are the engineering ones, i.e., they are extracted by dividing the total force applied on the side of the cube whose displacement is controlled by its initial surface which is equal to unity. The corresponding strains are also the engineering ones obtained by dividing the total applied displacement by the initial side length of the cube which is unity again.

In order to compare the four geometries, we show in Figs. 7 and 8 uniaxial compression simulations for relative densities $\rho = 0.42, 0.33$. All geometries (but the Gyroid) have been tested in all three normal cubic directions, which corresponds to three different realizations given their randomness. They all show a fairly small dispersion along these three directions indicating a rather converged macroscopic material response. In particular, the M-Voronoi and RSA geometries exhibit a relatively good isotropic response[5] even at large strains, while the

[5] The use of "cubic symmetry" is obviously more rigorous than the use of "isotropic". Nonetheless, given the randomness of the solids, the word isotropy is used with a slight abuse of notation.

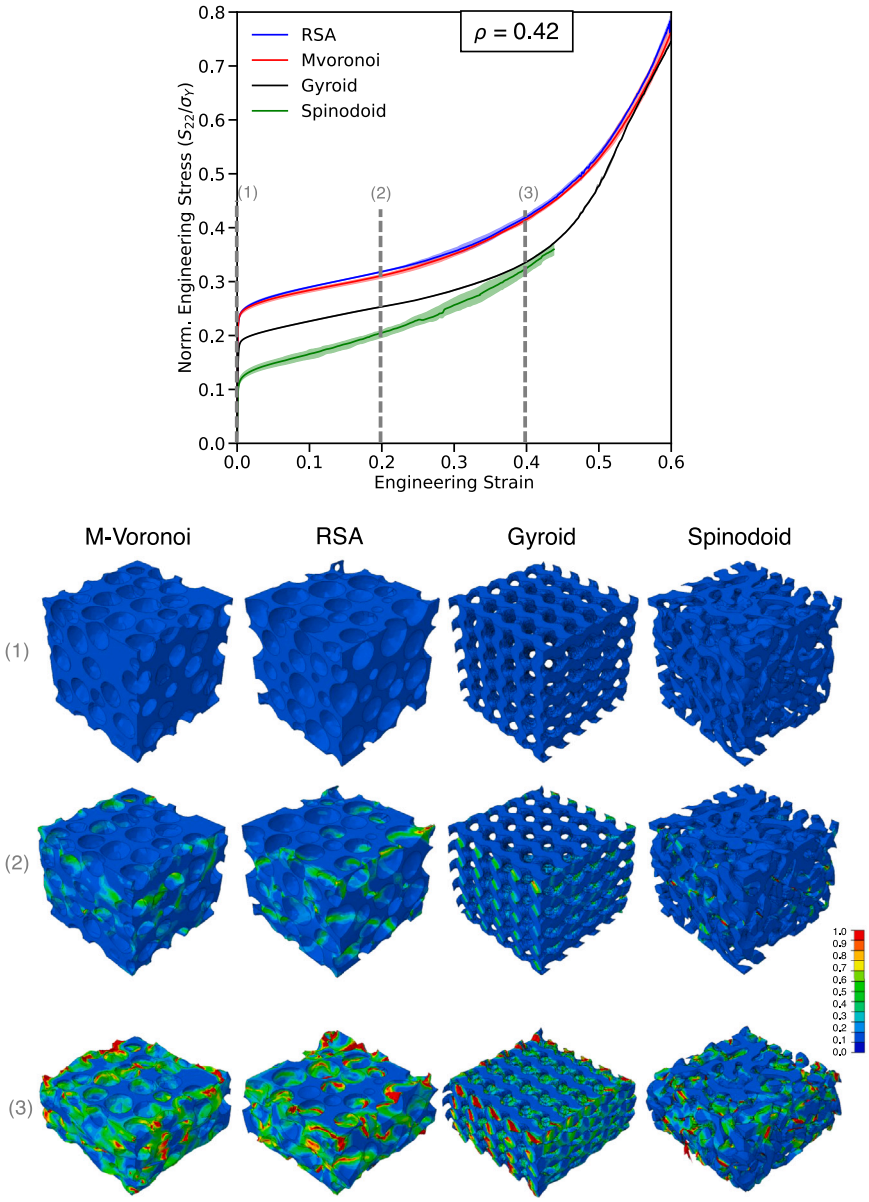

Fig. 7. Large strains compression engineering stress and strain curves for M-Voronoi, RSA, Gyroid and Spinodoid geometries with relative density $\rho = 0.42$. Deformed geometries at three intermediate strain levels, denoted by (1), (2) and (3) are displayed at the bottom. The color bar indicates the equivalent accumulated plastic strain values.

Spinodoid is slightly more dispersive and thus less isotropic (which is in accord with the results found in Fig. 5c). In turn, the Gyroid geometry has a perfect cubic symmetry and thus along the main cubic directions, the response is exactly equivalent, exhibiting no dispersion. Interestingly, the yield stress and large strain plastic response of the M-Voronoi and RSA geometries are almost identical and much higher than the Gyroid and Spinodoid geometries. This result shows clearly that randomness as such is not enough to achieve enhanced mechanical (or other) properties since Gyroid overall provides stiffer responses than the random Spinodoid one. The Spinodoid geometries lead to the lowest yield stress and overall flow response at large strains, albeit exhibiting a larger hardening rate. They also seem to start densification somewhat earlier than the rest of the geometries considered here. Unfortunately, we were unable to continue the simulations beyond the overall strains of 0.45 for the Spinodoid geometry, which was found to be by far the most challenging one to mesh and simulate with FE.

In order to gain further insight, we also include the deformations of the four geometries at three different strain levels, denoted by (1), (2), and (3) in Figs. 7 and 8. By plotting the accumulated equivalent plastic strain (PEEQ in Abaqus notation) of the deformed geometries, we observe that the random features of the M-Voronoi and RSA geometries such as random void size, shape, position, and ligament thickness, lead to a diffuse distribution of plastic localization at various unconnected zones of the specimen. This seems to be a rather interesting enhancement when compared with existing open-cell foams which tend to localize in long wavelength bands (Barnes et al., 2014; Gaitanaros and Kyriakides, 2014). In those cases, the ligaments have a more uniform size distribution, leading to easy collapse paths throughout the specimen despite their random distribution. Of course, this is expected to be the case as well in the M-Voronoi at much lower densities (less than 0.05).

For a better understanding, we show in Fig. 9 corresponding mid-plane cross-sectional contours of the plastic shear ϵ^p_{12} and normal ϵ^p_{22} strains. We observe that the M-Voronoi and RSA exhibit multiple low deformation *pockets* and a more diffuse straining but without evidence of long wavelength localization. By contrast, the Gyroid has, by construction, a periodic distribution of straining. In all but the Spinodoid geometry, we observe also a rather pronounced presence

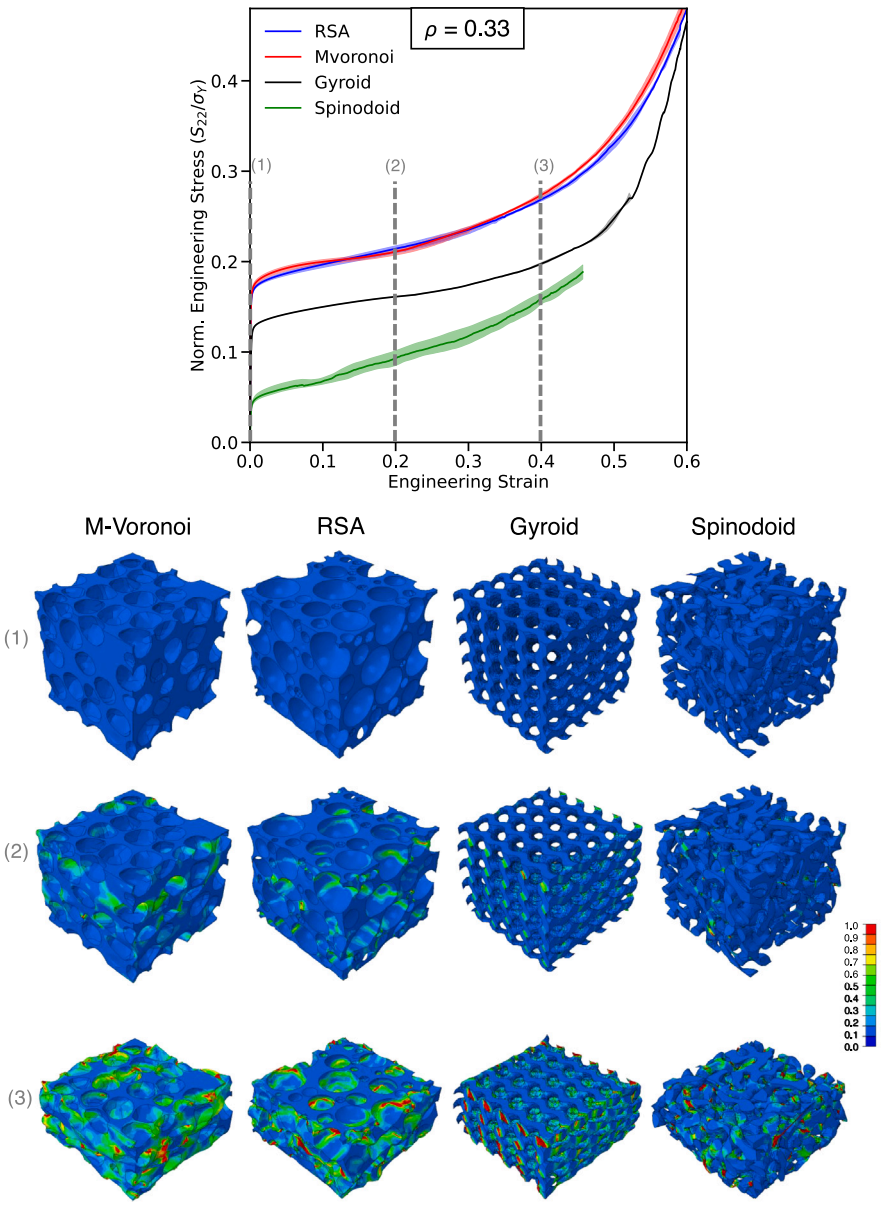

Fig. 8. Large strains compression engineering stress and strain curves for M-Voronoi, RSA, Gyroid and Spinodoid geometries with relative density $\rho = 0.33$. Deformed geometries at three intermediate strain levels, denoted by (1), (2) and (3) are displayed at the bottom. The color bar indicates the equivalent accumulated plastic strain values.

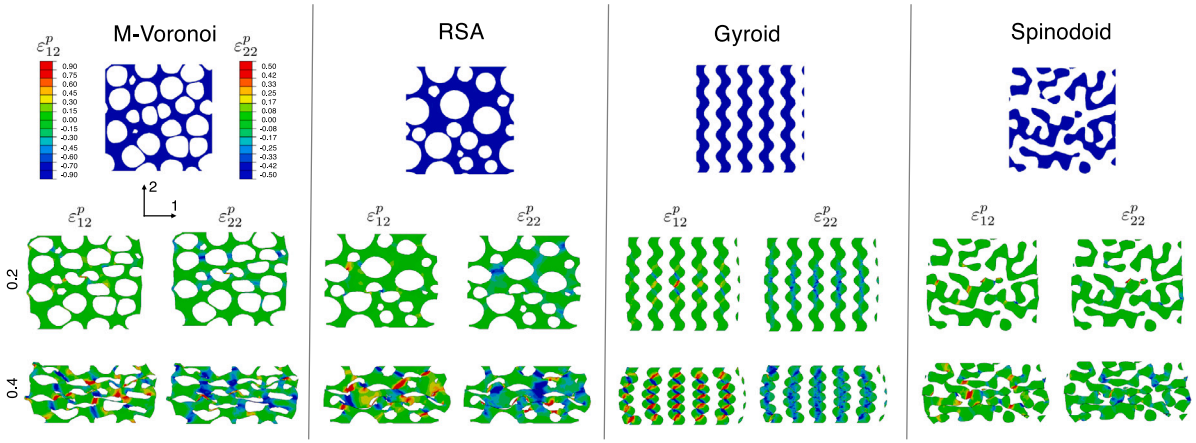

Fig. 9. Two-dimensional deformed cross-sections for M-Voronoi, RSA, Gyroid and Spinodoid geometries with relative density $\rho = 0.42$. Deformed geometries at two intermediate macroscopic strain levels 0.2 and 0.4 (see Fig. 7). The color bars indicate the shear ϵ^p_{12} and normal ϵ^p_{22} plastic strains.

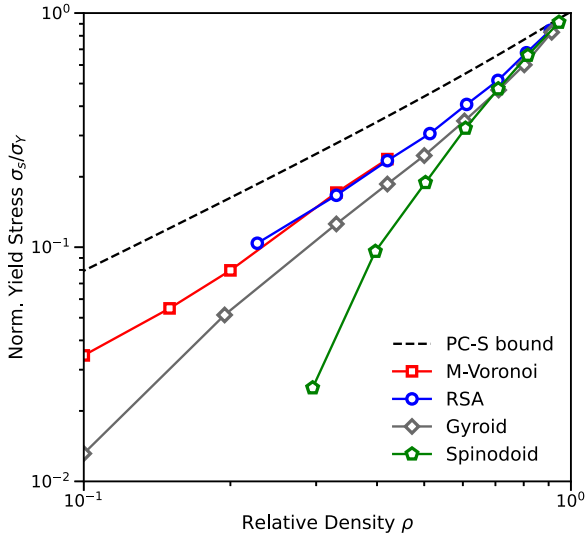

Fig. 10. Yield stress results for the M-Voronoi, RSA, Gyroid and Spinodoid geometries as a function of the relative density ρ obtained by FE simulations. For comparison purposes, we also include the Ponte-Castañeda-Suquet (PC-S) bound for stress triaxiality $-1/3$, which is that for uniaxial compression.

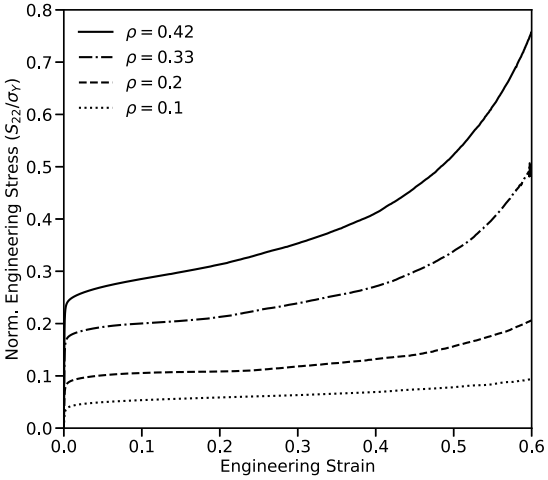

Fig. 11. Large strains compression simulations for M-Voronoi geometries at four different relative densities $\rho = 0.42$, 0.33, 0.20, and 0.1. The values of stress and strain correspond to their nominal or engineering values.

of plastic shear strains ϵ^p_{12}, which implies that one cannot see such structures neither as stretching nor as bending type. In turn, the Gyroid and Spinodoid exhibit multiple empty regions at the cross-sectional level, which is a direct consequence of the void connectivity in the matrix (Bonatti and Mohr, 2019; Zerhouni et al., 2021). In particular, contrary to the Gyroid, the Spinodoid seems to localize most of the straining in a few thin ligaments and due to the open porosity is not able to re-transmit the forces to neighboring undeformed domains. This explains to a large extent the overall soft response of this geometry.

Such responses as that of the periodic Gyroid are fairly known to occur also in other periodic geometries including trusses, lattices, and plate-based architected materials. A critical issue of periodic geometries, that should be taken into account during manufacturing, is their imperfection sensitivity which is not present in random materials as the RSA, M-Voronoi and Spinodoids. At this point, it is important to mention that despite their stiff response, M-Voronoi and RSA are closed-cell porous materials and thus their realizability by use of the current 3D-printing technology is yet not feasible, unless a very soft support material is used in the void phase (Tarantino et al., 2019). In the latter case, the support material adds to the overall weight thus making the structure not lightweight. Nevertheless, new 3D-printing technologies with movable printing bases are currently being developed which may allow in the future the 3D-printing of enhanced materials such as the M-Voronoi and RSA ones. Moreover, more traditional foaming techniques can also result in M-Voronoi type materials.

Fig. 10 reports collective yield stress data as a function of the relative density ρ. Those data are extracted by use of a 0.2% offset strain approach and small strain uniaxial compression elastoplastic simulations (with strain amplitude not exceeding 2%). We have verified that the small strain implicit calculations and large strain explicit calculations have negligible differences at such low strain amplitudes. For comparison purposes, we also show the modified estimate of Suquet (1993), which is very close in this case of low stress triaxiality to the bound of Ponte Castañeda (1991), denoted as PC-S bound in Fig. 10. Again, we observe that the M-Voronoi and RSA almost overlap, while the Gyroid leads to lower yield stress than the other two. The Spinodoid exhibits a very sharp drop near $\rho \sim 0.3$, similar to its elastic response.

For completeness, Fig. 11 presents the stress–strain response of the M-Voronoi geometries at four different relative densities $\rho = 0.42, 0.33, 0.20, 0.10$. As intuitively expected, the larger the density, the stiffer the flow response and the higher the computed yield stress. Another observation is that the hardening rate of the stress–strain response decreases with decreasing relative densities. The reason for this can be explained by the fact that at higher relative densities, the void walls establish contact earlier than for lower densities and thus hardening appears earlier. Moreover, at higher densities, the local deformation of the matrix is triaxial with important shearing, while at lower densities the deformation becomes of a more bending and stretching type. This last set of results shows that the M-Voronoi geometries are fairly robust to mesh and simulate at large strains and for a wide range of relative densities considered here. This makes them excellent candidates for analyzing the response of industrially manufactured closed-cell foams.

We close by noting that both the M-Voronoi and the Gyroid, two of the microstructures that allowed us to reach very low densities become increasingly difficult to simulate in elasto-plasticity (elasticity is more forgiving in that sense) at $\rho < 0.1$ with 3D finite elements due to strong deformation localization. This is somewhat expected and beyond this point, one should resort to more approximate numerical techniques using shell elements. The M-Voronoi for $\rho < 0.1$ resembles very closely the standard eroded Voronoi materials, which are easier to use with shell elements. Instead, the present M-Voronoi can be 3D-printed using the existing approach even at low densities depending of course on the accuracy of the 3D-printer at hand. The Gyroid, on the other hand, is less trivial to analyze at lower relative densities with the current approach and one needs to use a shell type of approach (see for instance Hsieh et al. 2019).

5.2. Results: simple shear

Similar results to those in uniaxial compression have also been obtained when the porous geometries are subjected to simple shear loading. We carry out the simulation by applying a displacement tangential to one of the cube surfaces, while blocking the remaining two components. At the opposite surface, we apply clamped boundary conditions. The remaining side surfaces of the cube are left traction-free. Such a load again mimics rather closely realistic conditions in the laboratory and thus experimental data in the literature. Fig. 12 shows such results for the four considered geometries at two different relative densities $\rho = 0.42, 0.33$. In this case, the stress response of the M-Voronoi and RSA are fairly close to each other only initially, whereas at larger strains the RSA exhibits a softer response. Interestingly, the Gyroid geometry lies much closer to the RSA curves (contrary to the case of uniaxial compression) indicating a significant anisotropic response

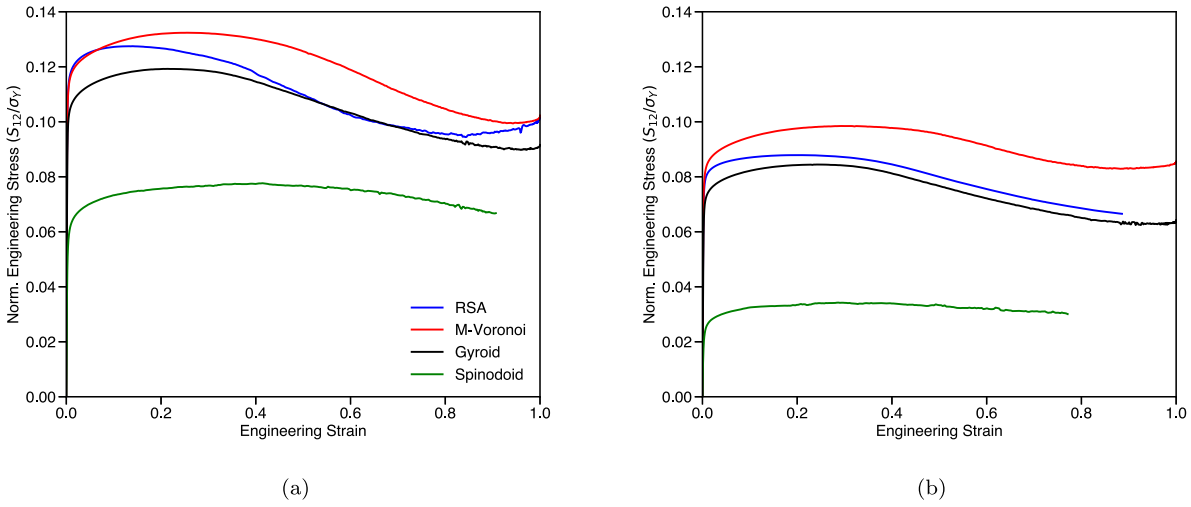

Fig. 12. Simple shear response for M-Voronoi, RSA, Gyroid and Spinodoid geometries for relative densities (a) $\rho = 0.42$ and (b) $\rho = 0.33$.

of the earlier. This is somewhat expected since simple shear can be understood as pure shear tension/compression (at least initially at small strains) along the diagonal direction, which is naturally stiffer than the normal directions in the Gyroid geometries. Finally, the Spinodoid geometry response remains substantially lower than the rest of the geometries analyzed here.

6. Conclusions

In this work, we have developed a mechanically-grown geometry generation method based on nonlinear elastic finite strain computations to create M-Voronoi porous (or composite) materials that span almost the entire relative density range from 1 all the way to 0.01. The nonlinear elastic energy minimization of the matrix phase together with the initial RSA geometry has led to random but smooth, convex void shapes and sizes and non-uniform intervoid ligament sizes in the M-Voronoi material. This enhanced randomness has been found to be beneficial for the mechanical properties of the porous material both in terms of stiffness and flow stress.

By comparison with other geometries, random and periodic, we have shown unambiguously that randomness may lead to enhanced mechanical properties but is not a panacea. It actually depends on the type of features employed, their smoothness and perhaps more importantly how random they are. Specifically, we have found that M-Voronoi and polydisperse RSA with spherical voids almost coincide in the range that RSA is realizable and attainable (i.e. relative densities larger than 0.2) and exhibit the stiffest and highest flow stress response. This has been attributed to variable void size and shape (for the M-Voronoi) and the complex shape and non-uniform thickness of the intervoid regions that have non-convex polyhedral shapes. These features lead to a diffuse map of strain localization instead of long wavelength localization bands that span the entire specimen.

In turn, the Gyroid TPMS periodic geometry exhibits lower stiffness, yield and flow stress than the two previously-mentioned random geometries. Nevertheless, its simplicity in design is an advantage over the M-Voronoi material. The RSA method on the other hand is fairly simple and extremely fast to use but like the Gyroid, it is difficult to reach low to very low relative densities. Finally, the Spinodoid geometry is the less resistant one both in terms of elasticity and yield/flow stress. In addition, it reaches percolation and thus zero stiffness at relative densities just below $\rho < 0.3$. On the other hand, Spinodoids and Gyroids are open-cell geometries with rather well-controlled connectivity features, thus offering potential advantages in thermal or diffusion transport applications. Recently, the RSA geometry has been extended to include connectivity allowing for non-zero permeability properties maintaining better mechanical stiffness than the thresholded Gaussian Random Fields (a cousin of Spinodoids) (Zerhouni et al., 2021).

As a byproduct of the M-Voronoi generation process, a novel and versatile remeshing algorithm has also been proposed that allows to read and remesh complex orphan meshes. This algorithm uses Python scripting and is extremely fast irrespective of the size and detailed features of the mesh analyzed. It has been recently used to carry out numerical finite strain simulations of particle reinforced composites which require extensive remeshing and stress mapping (Luo et al., 2023). Remeshing has been shown to be absolutely necessary to reach lower densities as well as to provide a good quality mesh for the subsequent elasto-plastic simulations.

We close by noting that, similar to Gyroid and Spinodoids, the proposed M-Voronoi and older RSA geometries can be readily extended to obtain composite materials with two or more phases (Papadioti et al., 2016; Bele et al., 2017) thus allowing them to reach very high volume fraction of inclusions. This could be of interest in applications beyond mechanics such as magnetic, piezoelectric or magneto-electric composites (Mukherjee et al., 2021; Lopez-Donaire et al., 2022).

CRediT authorship contribution statement

Z. Hooshmand-Ahoor: Conceptualization, Data curation, Formal analysis, Investigation, Methodology, Software, Validation, Visualization, Writing – original draft, Writing – review & editing. **H. Luo:** Formal analysis, Methodology, Software. **K. Danas:** Conceptualization, Investigation, Methodology, Project administration, Resources, Supervision, Validation, Writing – review & editing.

Declaration of competing interest

The authors declare that they have no known competing financial interests or personal relationships that could have appeared to influence the work reported in this paper.

Data availability

Data will be made available on request.

Acknowledgments

The authors would like to thank Prof. Julie Diani, LMS, CNRS, Ecole Polytechnique and Prof. Gabriella Tarantino, LMPS, University of Paris-Saclay for extremely helpful discussions throughout this study. Z.H.A acknowledges the support of the Ecole Polytechnique via a Monge scholarship. Also, Z.H.A. and K.D. acknowledge the support from the European Research Council (ERC) under the European Union's Horizon 2020 research and innovation program (grant agreement No 636903 and No 101081821). H.L. benefited from the support of the Chair Modeling advanced polymers for innovative material solutions led by the Ecole Polytechnique (l'X), France and the Fondation de l'Ecole Polytechnique, France and sponsored by Arkema, France. The codes used for the present work may become available upon reasonable request to the authors.

Appendix A. Algorithms for remeshing a 3D orphan mesh by constructing the geometry

Nomenclature:

- n: total number of nodes in the orphan mesh
- m: total number of elements in the orphan mesh
- h: the number of nodes per element
- r: the number of nodes per element surface
- f: the number of free surfaces
- N: the number of volumes
- $\mathbb{N}_{n\times 3}$: matrix containing the nodes coordinates
- $\mathbb{M}_{m\times h}$: matrix containing the elements information
- $\mathbb{S}_{f\times r}$: matrix containing the nodes of free surfaces
- $s_i = \mathbb{S}(i, 1:r)$: the individual identified free surface
- $S = \{s_1, s_2, \dots, s_f\}$: the group of all identified free surface
- $V = \{v_1, v_2, \dots, v_N\}$: the group of all closed volumes
- S_i All the free surfaces on volume i
- P_i All the free nodes on volume i

Algorithm 1 Finding the free surfaces of an orphan mesh.

Initialize the algorithm with the number of free surfaces $f = 0$
for $p = 1, m$ **do**
  for $q = 1, h$ **do**
    $ref = [\mathbb{M}(p,q), \mathbb{M}(p,q+1), \mathbb{M}(p,q+2)]$
    for u=1, number of elements with common node q **do**
      for $v = 1, h$ **do**
        $comp = [\mathbb{M}(u,v), \mathbb{M}(u,v+1), \mathbb{M}(u,v+2)]$
        if $ref = comp$ **then**
          goto 3
        else
          if h=4 **then** ▷ Linear tetrahedron element
            $\mathbb{S}(f,:) = [\mathbb{M}(p,q), \mathbb{M}(p,q+1), \mathbb{M}(p,q+2)]$
            $f \leftarrow f + 1$
          else if h=10 **then** ▷ Quadratic tetrahedron element
            $\mathbb{S}(f,:) = [\mathbb{M}(p,q), \mathbb{M}(p,q+1), \mathbb{M}(p,q+2),$ midnode12, midnode23, midnode31 $]$
            $f \leftarrow f + 1$
          end if
        end if
      end for
    end for
  end for
end for

Algorithm 2 Constructing 3D geometry by the identified free surfaces.

Initialize the algorithm with the number of identified volumes $N = 0$
for $s_i \in S = \{s_1, s_2, ..., s_f\}$ **do**
  if s_i is already investigated **then**
    goto 2
  else
    $N = N + 1$
    Add s_i to S_N ▷ S_N corresponds to the set of free surfaces in the current volume v_N
    Add the nodes on s_i to P_N ▷ P_N corresponds to the set of free nodes in the current volume v_N
    for $s_j \in$ the surfaces connected to the nodes in P_N **do**
      if s_j is already investigated **then**
        goto 9
      else
        Add s_j to S_N
        Add the nodes on s_j to P_N
        goto 9
      end if
    end for
  end if
  At this point all the free surfaces of the volume v_N are investigated.
  $v_N = \{P_N; S_N\}$ ▷ The nodes and the surfaces sets P_N and S_N construct the volume v_N
  Add v_N to V ▷ The volume v_N is added and we can start the construction of the next volume v_{N+1}, if there is any.
end for
N = number of identified volumes

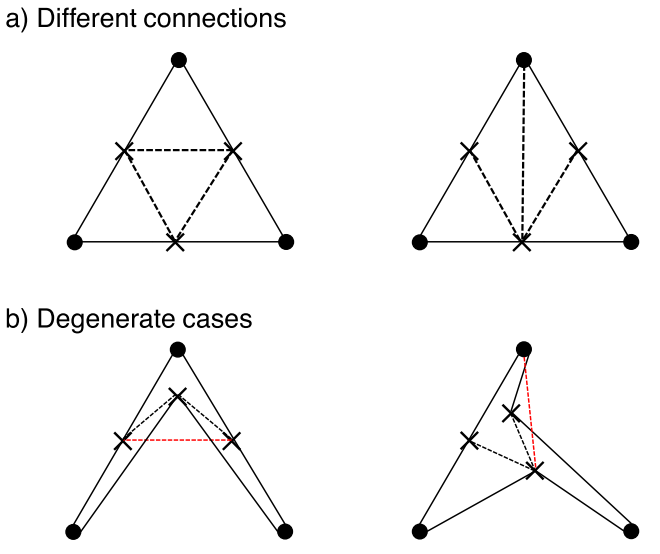

Fig. B.13. The limitations of the 3D remeshing algorithm in the case of quadratic elements. (a) The possible node connection methods for a free surface of a quadratic tetrahedral element type. We note that the nodes are not in the same plane. (b) The degenerate cases of each connection method when excessive element distortion exists. In both cases, the red line overlaps the neighboring elements.

Appendix B. Some issues with the remeshing technique

In spite of the flexibility of the proposed remeshing method, certain limitations exist and are important to be stated. The proposed remeshing method is applicable to all element types with linear order. Also in practice, one can approximate the quadratic elements with the corresponding linear type, by connecting the corner nodes and ignoring

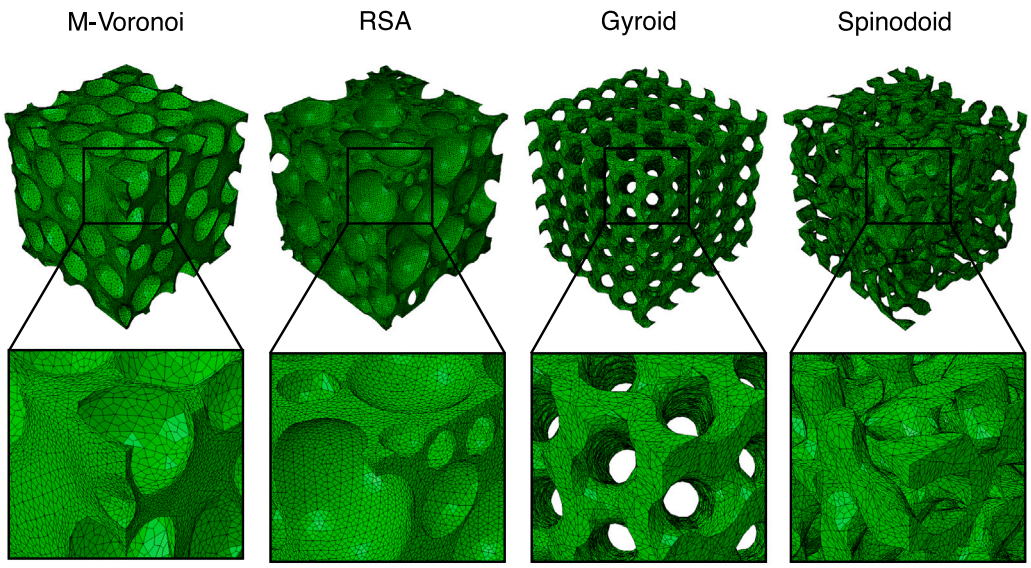

Fig. C.14. Examples of final hexahedral meshes used in the small and large strain elasto-plastic simulations.

the middle nodes. However, this will lead to a minor difference (< 3% depending on the mesh size) between the actual and reconstructed volume fraction of the embedded phases.

Specifically, the reconstruction algorithm is found to have limitations when dealing with quadratic elements under very large deformations. In contrast to linear elements, the points of a surface in a deformed 3D quadratic element do not lie on the same plane. As a result, in the case of very large deformations, one may run into different degenerate cases such as the ones shown in Fig. B.13b. In such cases, one can construct instead the deformed surface by ignoring the mid nodes and only connecting the corner nodes to define a single plane.

Specifically, in Fig. B.13a, two possible connection methods for points on a free element surface are shown, where the corner and middle nodes are represented by solid circles and crosses, respectively. It is important to note that the points are not on the same surface. The 3D surface is then constructed by connecting four triangular surfaces. It has been observed that both of the proposed connection methods can accurately (without any loss of volume fraction) construct the deformed geometry up to large distortions of the elements. However, large deformations in the geometry, whether local or global, may cause the elements to be distorted such that both approaches will not work. Fig. B.13b represents the degenerate cases of each approach. In both cases, the red line overlaps the neighboring elements and subsequently, the geometry construction will be unsuccessful. Such distortions are mainly present at low densities $\rho < 0.2$. In order to avoid such limitations, two approaches can be followed: first, the simulation can be stopped before excessive element distortion and the deformed mesh can be remeshed (with or without stress mapping) to improve the quality of the elements and second, the quadratic elements can be approximated by linear type. We note that the second approach will add a small error to the final volume fraction and might not work if the elements are highly distorted.

Appendix C. Examples of hexahedral meshes

Fig. C.14 shows examples of the meshes used to carry out the small and large strain elasto-plastic simulations in the present work. The exhibited meshes comprise approximately 10^6, 8-node, isoparametric, hexahedral, conformal elements. The meshing is carried out using first a tetrahedral automatic meshing option and subsequently a hexahedra subdivision method in `Gmsh`.

References

Amani, Y., Takahashi, A., Chantrenne, P., Maruyama, S., Dancette, S., Maire, E., 2018. Thermal conductivity of highly porous metal foams: Experimental and image based finite element analysis. Int. J. Heat Mass Transfer 122, 1–10.

Andrew, J.J., Alhashmi, H., Schiffer, A., Kumar, S., Deshpande, V.S., 2021. Energy absorption and self-sensing performance of 3d printed cf/peek cellular composites. Mater. Des. 208, 109863.

Anoukou, K., Brenner, R., Hong, F., Pellerin, M., Danas, K., 2018. Random distribution of polydisperse ellipsoidal inclusions and homogenization estimates for porous elastic materials. Comput. Struct. 210, 87–101.

Ashby, M.F., Gibson, L.J., 1997. Cellular Solids: Structure and Properties. Press Syndicate of the University of Cambridge, Cambridge, UK, pp. 175–231.

Balit, Y., Margerit, P., Charkaluk, E., Constantinescu, A., 2021. Crushing of additively manufactured thin-walled metallic lattices: Two-scale strain localization analysis. Mech. Mater. 160, 103915.

Barnes, A., Ravi-Chandar, K., Kyriakides, S., Gaitanaros, S., 2014. Dynamic crushing of aluminum foams: Part I – experiments. Int. J. Solids Struct. 51, 1631–1645.

Bele, E., Goel, A., Pickering, E., Borstnar, G., Katsamenis, O., Pierron, F., Danas, K., Deshpande, V., 2017. Deformation mechanisms of idealised cermets under multi-axial loading. J. Mech. Phys. Solids 102, 80–100.

Bonatti, C., Mohr, D., 2019. Mechanical performance of additively-manufactured anisotropic and isotropic smooth shell-lattice materials: Simulations & experiments. J. Mech. Phys. Solids 122, 1–26.

Cignoni, P., Callieri, M., Corsini, M., Dellepiane, M., Ganovelli, F., Ranzuglia, G., et al., 2008. Meshlab: an open-source mesh processing tool. In: Eurographics Italian Chapter Conference. Salerno, Italy, pp. 129–136.

Combescure, C., Elliott, R.S., Triantafyllidis, N., 2020. Deformation patterns and their stability in finitely strained circular cell honeycombs. J. Mech. Phys. Solids 142, 103976.

Combescure, C., Henry, P., Elliott, R.S., 2016. Post-bifurcation and stability of a finitely strained hexagonal honeycomb subjected to equi-biaxial in-plane loading. Int. J. Solids Struct. 88, 296–318.

Cooper, D.W., 1988. Random-sequential-packing simulations in three dimensions for spheres. Phys. Rev. A 38 (522).

de Francqueville, F., Gilormini, P., Diani, J., 2019. Representative volume elements for the simulation of isotropic composites highly filled with monosized spheres. Int. J. Solids Struct. 158, 277–286.

Dong, L., Deshpande, V., Wadley, H., 2015. Mechanical response of Ti–6Al–4v octet-truss lattice structures. Int. J. Solids Struct. 60, 107–124.

Feder, J., 1980. Random sequential adsorption. J. Theoret. Biol. 87, 237–254.

Fu, Y., Ogden, R., 2001. Nonlinear Elasticity: Theory and Applications. Cambridge University Press.

Fu, Y.B., Xie, Y.X., 2012. Effects of imperfections on localized bulging in inflated membrane tubes. Phil. Trans. R. Soc. A 370, 1896–1911.

Gahlen, P., Stommel, M., 2022. Modeling of the local anisotropic mechanical foam properties in polyisocyanurate metal panels using mesoscale fem simulations. Int. J. Solids Struct. 244–245, 111595.

Gaitanaros, S., Kyriakides, S., 2014. Dynamic crushing of aluminum foams: Part II – analysis. Int. J. Solids Struct. 51, 1646–1661.

Gaitanaros, S., Kyriakides, S., 2015. On the effect of relative density on the crushing and energy absorption of open-cell foams under impact. Int. J. Impact Eng. 82, 3–13.
Gaitanaros, S., Kyriakides, S., Kraynik, A.M., 2012. On the crushing response of random open-cell foams. Int. J. Solids Struct. 49, 2733–2743, Proceedings of International Union of Theoretical and Applied Mechanics Symposium.
Geslin, P.A., Buchet, M., Wada, T., Kato, H., 2019. Phase-field investigation of the coarsening of porous structures by surface diffusion. Phys. Rev. Mater. 3, 083401.
Geuzaine, C., Remacle, J.F., 2009. Gmsh: A 3-d finite element mesh generator with built-in pre-and post-processing facilities. Internat. J. Numer. Methods Engrg. 79, 1309–1331.
Ghazi, A., Berke, P., Tiago, C., Massart, T., 2020. Computed tomography based modelling of the behaviour of closed cell metallic foams using a shell approximation. Mater. Des. 194, 108866.
Gong, L., Kyriakides, S., 2005. Compressive response of open cell foams part II: Initiation and evolution of crushing. Int. J. Solids Struct. 42, 1381–1399.
Hashin, Z., Shtrikman, S., 1963. A variational approach to the theory of the elastic behaviour of multiphase materials. J. Mech. Phys. Solids 11, 127–140.
Hill, R., 1963. Elastic properties of reinforced solids: Some theoretical principles. J. Mech. Phys. Solids 11, 357–372.
Hooshmand-Ahoor, Z., Tarantino, M., Danas, K., 2022. Mechanically-grown morphogenesis of voronoi-type materials: Computer design 3d-printing and experiments. Mech. Mater. 104432, 173.
Hsieh, M.T., Endo, B., Zhang, Y., Bauer, J., Valdevit, L., 2019. The mechanical response of cellular materials with spinodal topologies. J. Mech. Phys. Solids 125, 401–419.
Jones, A., Leary, M., Bateman, S., Easton, M., 2021. Tpms designer: A tool for generating and analyzing triply periodic minimal surfaces. Softw. Impacts 10, 100167.
Kanit, T., Forest, S., Galliet, I., Mounoury, V., Jeulin, D., 2003. Determination of the size of the representative volume element for random composites: statistical and numerical approach. Int. J. Solids Struct. 40, 3647–3679.
Kumar, S., Tan, S., Zheng, L., Kochmann, D.M., 2020. Inverse-designed spinodoid metamaterials. npj Comput. Mater. 6, 1–10.
Lopez-Donaire, M.L., de Aranda-Izuzquiza, G., Garzon-Hernandez, S., Crespo-Miguel, J., la Torre, M.F., Velasco, D., Garcia-Gonzalez, D., 2022. Computationally guided diw technology to enable robust printing of inks with evolving rheological properties. Adv. Mater. Technol. 2201707.
Lopez-Pamies, O., Goudarzi, T., Danas, K., 2013. The nonlinear elastic response of suspensions of rigid inclusions in rubber: Ii—a simple explicit approximation for finite-concentration suspensions. J. Mech. Phys. Solids 61, 19–37.
Luan, S., Kraynik, A.M., Gaitanaros, S., 2022. Microscopic and macroscopic instabilities in elastomeric foams. Mech. Mater. 164, 104124.
Lubachevsky, B.D., Stillinger, F.H., 1990. Geometric properties of random disk packings. J. Statist. Phys. 60, 561–583.
Lubachevsky, B.D., Stillinger, F.H., Pinson, E.N., 1991. Disks vs. spheres: Contrasting properties of random packings. J. Stat. Phys. 64, 501–524.
Luo, H., Hooshmand-Ahoor, Z., Danas, K., Diani, J., 2023. Numerical estimation via remeshing and analytical modeling of nonlinear elastic composites comprising a large volume fraction of randomly distributed spherical particles or voids. Eur. J. Mech. A Solids 101, 105076.
Maskery, I., Aboulkhair, N., Aremu, A., Tuck, C., Ashcroft, I., 2017. Compressive failure modes and energy absorption in additively manufactured double gyroid lattices. Addit. Manuf. 16, 24–29.
Mbiakop, A., Constantinescu, A., Danas, K., 2015. An analytical model for porous single crystals with ellipsoidal voids. J. Mech. Phys. Solids 84, 436–467.
Michel, J., Lopez-Pamies, O., Ponte Castañeda, P., Triantafyllidis, N., 2007. Microscopic and macroscopic instabilities in finitely strained porous elastomers. J. Mech. Phys. Solids 55, 900–938.
Michel, J.C., Moulinec, H., Suquet, P., 1999. Effective properties of composite materials with periodic microstructure: a computational approach. Comput. Methods Appl. Mech. Engrg. 172, 109–143.
Moraleda, J., Segurado, J., Llorca, J., 2007. Finite deformation of porous elastomers: a computational micromechanics approach. Phil. Mag. 87, 5607–5627.
Mukherjee, D., Rambausek, M., Danas, K., 2021. An explicit dissipative model for isotropic hard magnetorheological elastomers. J. Mech. Phys. Solids 151, 104361.
Neumann, M., Stenzel, O., Willot, F., Holzer, L., Schmidt, V., 2020. Quantifying the influence of microstructure on effective conductivity and permeability: Virtual materials testing. Int. J. Solids Struct. 184, 211–220.
Papadioti, I., Danas, K., Aravas, N., 2016. A methodology for the estimation of the effective yield function of isotropic composites. Int. J. Solids Struct. 87, 120–138.
Papka, S., Kyriakides, S., 1998. Experiments and full-scale numerical simulations of in-plane crushing of a honeycomb. Acta Mater. 46, 2765–2776.
Pierard, O., Gonzalez, C., Segurado, J., Llorca, J., Doghri, I., 2007. Micromechanics of elasto-plastic materials reinforced with ellipsoidal inclusions. Int. J. Solids Struct. 44, 6945–6962.
Ponte Castañeda, P., 1991. The effective mechanical properties of nonlinear isotropic composites. J. Mech. Phys. Solids 39, 45–71.
Portela, C.M., Vidyasagar, A., Krödel, S., Weissenbach, T., Yee, D.W., Greer, J.R., Kochmann, D.M., 2020. Extreme mechanical resilience of self-assembled nanolabyrinthine materials. Proc. Natl. Acad. Sci. 117, 5686–5693.
Roberts, A., Garboczi, E., 2001. Elastic moduli of model random three-dimensional closed-cell cellular solids. Acta Mater. 49, 189–197.
Schoen, A.H., 1970. Infinite periodic minimal surfaces without self-intersections. In: NASA Technical Reports.
Schwarz, H.A., 1972. Gesammelte mathematische abhandlungen. Volume 260. American Mathematical Soc..
Segurado, J., Llorca, J., 2002. A numerical approximation to the elastic properties of sphere-reinforced composites. J. Mech. Phys. Solids (50).
Simone, A., Gibson, L., 1998. Effects of solid distribution on the stiffness and strength of metallic foams. Acta Mater. 46, 2139–2150.
Soyarslan, C., Bargmann, S., Pradas, M., Weissmüller, J., 2018. 3D stochastic bicontinuous microstructures: Generation, topology and elasticity. Acta Mater. 149, 326–340.
Soyarslan, C., Blümer, V., Bargmann, S., 2019. Tunable auxeticity and elastomechanical symmetry in a class of very low density core–shell cubic crystals. Acta Mater. 177, 280–292.
Spyrou, L., Brisard, S., Danas, K., 2019. Multiscale modeling of skeletal muscle tissues based on analytical and numerical homogenization. J. Mech. Behav. Biomed. Mater. 92, 97–117.
Su, B.Y., Jang, W.Y., 2022. The microstructure characterization and elastic properties of closed-cell foams. Int. J. Solids Struct. 257, 111700, Special Issue in the honour Dr Stelios Kyriakides.
Suquet, P., 1993. Overall potentials and extremal surfaces of power law or ideally plastic composites. J. Mech. Phys. Solids 41, 981–1002.
Symons, D.D., Fleck, N.A., 2008. The imperfection sensitivity of isotropic two-dimensional elastic lattices. J. Appl. Mech. (75).
Tarantino, M., Zerhouni, O., Danas, K., 2019. Random 3d-printed isotropic composites with high volume fraction of pore-like polydisperse inclusions and near-optimal elastic stiffness. Acta Mater. 175, 331–340.
Torquato, S., 2002. Random Heterogeneous Materials: Microstructure and Macroscopic Properties. Springer, New York.
Wang, L., Limodin, N., El Bartali, A., Charkaluk, E., 2021. Coupling of x-ray computed tomography and surface in situ analysis combined with digital image correlation method to study low cycle fatigue damage micromechanisms in lost foam casting a319 alloy. Fatigue Fract. Eng. Mater. Struct. 44, 916–932.
Warren, W.E., Kraynik, A.M., 1997. Linear elastic behavior of a low-density Kelvin foam with open cells. J. Appl. Mech. 64, 787–794.
Wejrzanowski, T., Skibinski, J., Szumbarski, J., Kurzydlowski, K., 2013. Structure of foams modeled by Laguerre–Voronoi tessellations. Comput. Mater. Sci. 67, 216–221.
Zerhouni, O., Brisard, S., Danas, K., 2021. Quantifying the effect of two-point correlations on the effective elasticity of specific classes of random porous materials with and without connectivity. Internat. J. Engrg. Sci. 166, 103520.
Zerhouni, O., Tarantino, M., Danas, K., 2019. Numerically-aided 3d printed random isotropic porous materials approaching the Hashin-Shtrikman bounds. Composites B 156, 344–354.